Quantification of Damage and its Effects on the Compressive Strength of an Advanced Ceramic

Erez Krimsky[a,b], K.T. Ramesh[a,b], M. Bratcher[c], M. Foster[c], James David Hogan[d,*]

[a]*Hopkins Extreme Materials Institute, The Johns Hopkins University, Baltimore, MD 21218, USA*
[b]*Department of Mechanical Engineering, The Johns Hopkins University, Baltimore, MD 21218, USA*
[c]*U.S. Army Research Laboratory, Aberdeen Proving Ground, Maryland 21005, USA*
[d]*Department of Mechanical Engineering, The University of Alberta, Edmonton, AB T6G 2R3, Canada*

Abstract

An understanding of the dynamic failure of damaged ceramics is important in protection applications, where the interaction of the projectile with cracked material is a contributing factor in the overall system performance. In this paper, we investigate the effects of pre-existing internal cracks on the quasi-static and dynamic compressive behavior of an advanced ceramic. We present experiments on a hot-pressed boron carbide in which internal cracks are generated through thermal shocking after which the initial material damage is quantified. Damage characterization was performed via Resonant Ultrasound Spectroscopy (RUS) and high-resolution Computed Tomography (CT). A computational procedure is developed to determine the three-dimensional structure of the internal crack network in the initially damaged material from a series of CT images. The failure and strength of the material is then evaluated experimentally. The uniaxial compressive strength of the predamaged boron carbide samples is determined under both quasistatic and dynamic loading scenarios and this is correlated with the pre-existing crack structure as determined by CT. Damaged samples were found to have average compressive strength of 1.14 GPa in quasistatic loading and 0.68 GPa in dynamic loading compared to 2.98 ± 0.6 GPa and 3.70 ± 0.3 GPa for pristine material, respectively. High speed photography employed during dynamic testing indicates that pre-existing cracks may lead to different failure mechanisms from what is normally seen in pristine material. Ultimately, these insights can be used to design improved materials that are more resistant to dynamic failure.

Keywords: microcracks; thermal shock; compressive fragmentation; brittle failure; experimental mechanics; advanced ceramics;

*Corresponding Author
Email address: jdhogan@ualberta.ca (James David Hogan)

Nomenclature

$\mathbf{B}$	initial binary image matrix
E	explanation for the abbreviation
$\bar{l}$	average measured grain size
$\mathbf{M}$	final binary image matrix
$\mathbf{M}'$	padded final binary image matrix
$\bar{s}$	average defect size
$\mathbf{S}$	integer image matrix
v_{shear}	shear wave speed
η	defect density
ν	Poisson's ratio
ρ	density
μ_{log}	disk size lognormal distribution mean
μ_n	disk size normal distribution mean
σ_{log}	disk size lognormal distribution standard deviation
σ_n	disk size normal distribution standard deviation

1. Introduction

Designing advanced ceramics for protection applications requires an understanding of failure and fragmentation mechanisms. These mechanisms have been shown to depend on material processing and specifics of the stress-state and strain-rate. Recent work has aimed to understand how the presence of internal fractures prior to loading affects the failure process [1] [2] [3], and the results suggest that pre-existing cracks will have a considerable effect on the material response of advanced ceramics. Studying the mechanical response of damaged material will help us understand the process of damage evolution in advanced ceramics. This paper presents an approach to quantitatively measure the degree of damage within an advanced ceramic and then to relate this to its compressive response.

Previous studies of advanced ceramics have focused on characterizing the size, shapes, and types of microstructural features which are believed to serve as fracture initiation points [4] [5] [6] [7]. Studies have also focused on characterizing grain sizes and shapes, as well as material anisotropy [8]. Significant work has also been performed to characterize the rate-dependence of compressive strength [9] [10] [11] [12]. Under quasistatic compression the most deleterious defects are activated first, leading to crack growth and sample failure [5]. Under dynamic compression, however, the rate of loading is such that additional defects are activated before substantial crack growth occurs from the most deleterious defects (given finite crack speeds), and so dynamic loading leads to the activation of more distributed damage.

As experimental work has shown the importance of loading-rate, microstructural features, and microcracks in the failure process, computational models have been developed to try to capture these dependencies [13] [14]. The micro-mechanical modeling approach, for example, incorporates pre-existing flaw distributions in the material [15], and defines damage based on an evolving scalar crack density parameter. Similar work by Hu and Ramesh has further extended this type of model to account for flaw orientations and a tensorial damage parameter [16]. Tonge and Ramesh [17] further extended this approach into a full constitutive model with a computational implementation for large-scale simulations of impact events. Other researchers, such as Johnson and Holmquist, have modeled damage and damage evolution through a heuristic approach. The JH2 model defines a set of constants that can be determined by fitting experimental data over a wide range of loading conditions [18]. This approach does not directly incorporate any microstructure or crack statistics, yet can have strong predictive power when parameters are fit to a sufficiently large data set.

Motivated by the need to better understand the behavior of damaged materials and provide experimental data for modelling damaged behavior of brittle materials [18] [19] [20], this paper explores the quasistatic and dynamic compressive behavior of pre-cracked boron carbide. To accomplish damaged states, we thermally shock cuboidal specimens to produce internal crack networks that are ~mm in length scale and of the order of the test specimens. These crack networks are characterized through X-Ray tomography and Matlab-based image processing and are linked with mechanical properties and mechanical behavior. Other studies have used thermal shocking and mechanical loading to produce internal cracking in specimens within confined test setups [1] [2]. In this paper, we use thermal shocking because it allows us to produce porosities of interests ($\sim$ 1 to 3%) and crack sizes that are resolvable in X-Ray tomography scans, thus allowing, for the first time, a quantified measure of cracking that can be coupled to mechanical testing. The use of thermal shocking to produce $\sim$ mm-sized cracked material also yields structural cracking sizes that are similar to those observed during impact into the same material [21], where understanding the impact behavior of this material is an overarching goal of this paper. In undertaking this research, attempts have been made to generate internal cracking through mechanical cycling, but this either resulted in too few and too small of cracks, or chipping at the specimen surface. Altogether, this work contributes to a limited data set in the literature for cracked specimens [1] [2] [22] [23], where the bulk of the work on advanced ceramics has focused on intact materials and resulting fragmentation [4] [21] [24] [25] [26] [27]. Understanding the behavior of materials for intermediate levels of damage is valuable in validating and improving models [16] [15] [17] [18] that can be used to design improved ceramic materials for, for example, ballistic impact, where fracture and fragmentation behaviors are important in their overall performance [28].

2. Material

The material in this study was a hot-pressed boron carbide (Coorstek, Inc.) with a Young's modulus of 430 GPa, a density of $2,510$ kg/m^3, a Poisson's ratio of 0.16 to 0.17, and a fracture toughness of 2.5 MPa $\sqrt{m}$. These values are provided by the manufacturer. The grain structure is equiaxed with an average grain size of 15 μm. Almost all the grain boundaries have a high misorientation angle ($> 15°$). This material has been used in previous studies by the authors and collaborators, where the focus has been on microstructural characterization [6], compressive strength and failure of intact forms [5] [8], compressive fragmentation [4], and impact fragmentation [21]. Additional details are provided in these references.

The boron carbide material was received as a tile (conceptualized in 1a with disk-like features in the figure meant to represent the carbonaceous inclusions presented later in b) with dimensions of 305 mm length, 254 mm in width, and 8 mm in thickness. For this study, rectangular prismatic boron carbide samples of approximate dimension $3.5 \times 4.0 \times 5.3$mm were machined from these larger tiles with the longest dimension being oriented along the hot-pressing or "through-thickness" (TT) direction. During sample machining, effort was made to minimize sub-surface damage by systematically polishing the edges from ~ 100 μm finish to a 2 μm finish following the cutting operation. Examination of X-ray tomography scans (shown later) reveals no clear evidence of sub-surface damage from machining in the cubes under consideration in the current investigation.

The inclusions and defects in the microstructure were characterized using a Zeiss optical microscope with an AxioCam MRC camera and a TESCAN MIRA3 field emis-

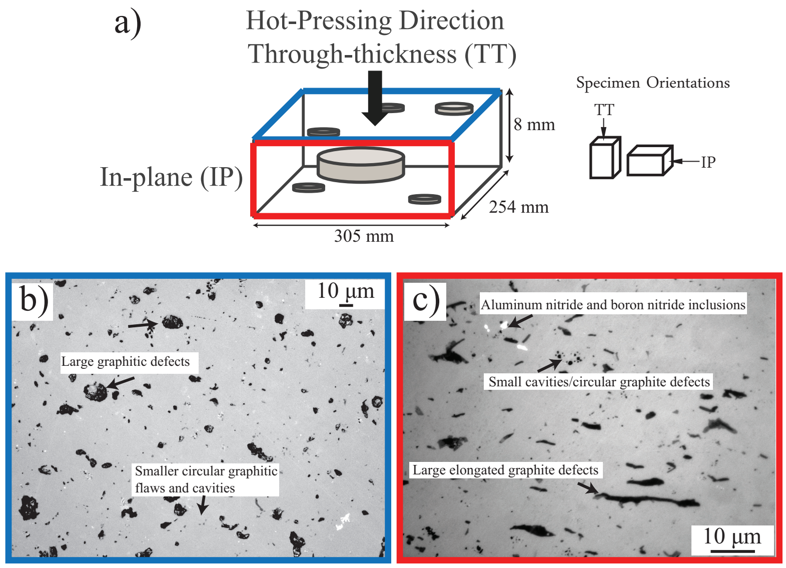

Fig. 1: (a) Conceptualized as-received tile of the hot-pressed boron carbide plate with through-thickness (TT) (in the hot-pressing direction) and in-plane directions (IP) labeled. Optical microscope images of the boron carbide microstructure in the (b) through-thickness (at 10 × magnification) and (c) in-plane direction (100× magnification) with the various types of inclusions and defects. [5]

sion Scanning Electron Microscope (SEM) equipped with a fully automated electron backscatter diffraction (EBSD) analysis system and Energy Dispersive Spectroscopy (EDS) capabilities. The word “defect” in this paper is used to denote a microstructural feature that may serve as a failure initiation site and “inclusion” is used to denote a feature that is not believed to contribute to failure (at least not under the stress states studied here). The processing-induced inclusions and defects are most easily seen in optical microscope images such as those shown in Fig. 1b and c. The image on the left is taken on the TT face, while the image on the right is taken on the IP face (note the different scale bars). Large, approximately circular, dark features are observed in the TT images in Fig. 1b. These have been confirmed to be carbonaceous in composition using EDS. Also highlighted in Fig. 1b are smaller and more circular features. These are primarily smaller graphitic defects, with other smaller features consisting of cavities/pores (confirmed with SEM/EDS). Brighter phases are also noted in Fig. 1b and these appear to be primarily comprised of aluminum nitride (AlN) and boron nitride (BN) (confirmed with SEM/EDS). These inclusions are faceted structures less than 20 μm in size, and are commonly observed at boron carbide grain boundaries.

Previous work has shown that graphitic disks in boron carbide are the microstructural features where fracture typically nucleates during failure in pristine (undamaged) specimens [5]. Again, these features are shown in the schematic representation of the as-received tile in Fig. 1a. The orientation, size, and spacing of these defects governs a variety of length scales that dictate rate dependence of the material strength [29]. These statistics are summarized in Table 2. The graphitic disk defect size was found to be well characterized by a lognormal distribution given by μ_{log} and σ_{log} whereas the defect orientation was found to be well characterized by a normal distribution given by μ_n and σ_n [5].

Material	$\bar{l}$ (μm)	η(#/m^2)	$\bar{s}$ (μm)	μ_{log} (μm)	σ_{log} (μm)	μ_n	σ_n
PAD Boron Carbide	16.0 ± 2.1	1.41×10^9	4.22 ± 2.54	1.30 ± 0.02	0.53 ± 0.02	0 ± 1°	20 ± 1°

Table I: Microstructure characteristics for pressure aided densification boron carbide, including $\bar{l}$: average measured grain size, η: defect density measured on the IP face for $s > 0.5\mu$m, $\bar{s}$: average defect size, μ_{log}, σ_{log}: disk size lognormal distribution parameters, μ_n, σ_n: disk orientation normal distribution parameters

For a material that already contains a significant number of flaws, it is not yet known exactly what effect the presence of these microstructure features will have upon the evolution of damage in a pre-damaged sample subjected to additional loading. We will explore this here.

3. Experimental Approach

Studies of damage evolution and the effects of internal cracking on the failure and strength of such materials [1] are limited. We use the approach described in Fig. 2 to capture the intermediate state of the material, with the intention of providing insight into dynamic damage evolution.

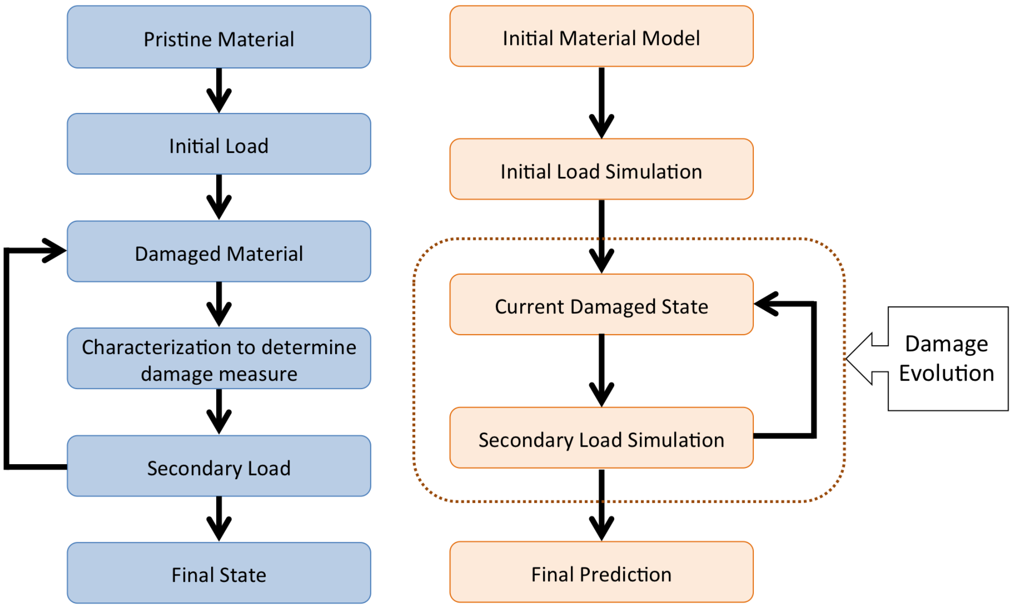

Fig. 2: Left: schematic showing the experimental process developed for this study. Traditional experiments go directly from the *initial load* to the *final state*. Right: schematic showing common computational procedure for simulating loading with damage evolution.

We achieve an intermediate damaged state by subjecting samples to an *initial load* that induces internal fracture without actually causing specimen fragmentation. The specimen is then characterized in this damaged state before an additional loading is provided. This process can be repeated until fragmentation occurs and the specimen has lost its load bearing capacity. The *pristine material* in our study is a sample of the boron carbide material described above. Although the specimen contains a variety of microstructural defects, it is considered to be free of damage until cracks have been induced by the initial (or primary) load. The *primary load* is performed via a thermal shock process described below. This leads to an intermediate *damaged material*. *Characterization* of this material provides a quantifiable *damage measure*. The characterization presented here was carried out via microscale CT to determine the internal crack structure and via resonant ultrasound spectroscopy to examine potential degradation of elastic properties. The secondary loading of this damaged sample is performed either via dynamic compressive testing with a Kolsky bar apparatus or through quasistatic compression with an MTS load frame system. The details of these tests are described below. If the secondary loading event does not fragment the sample, the process of characterization and loading can be repeated until a fragmented state is reached.

3.1. Thermal Shock

Material damage was induced via a thermal shock process. Previous studies on heated boron carbide with cooling on the boundary have shown that large thermal gradients lead to cracks propagating inward from the material boundary due to large tensile stresses [30]. For example, Chocron et. al. [1] investigated a thermal shock process through repeated heating and quenching on Pressure Assisted Densification (PAD) boron carbide and found that the extent of the crack propagation depends on the number of thermal cycles.

Five samples of boron carbide with approximate dimension $3.5 \times 4 \times 5.3$ mm were heated in a furnace in air. Samples were placed on small alumina tiles which could be easily manipulated with furnace tongs. The alumina tiles were placed on alumina foam blocks in the furnace. Samples were heated for ~ 1 hour to temperatures $550 - 850$°C. After heating, the alumina tiles were removed from the furnace and tipped over into a beaker of room temperature water thereby immersing the samples. Certain samples were run through two heat and quench cycles to increase the degree of internal cracking. The thermal cycling parameters of the samples can be found in Table 4.1. These are discussed later.

3.2. *Resonant Ultrasound Spectroscopy*

Pristine and thermally shocked samples were subjected to resonant ultrasound spectroscopy (RUS) to determine elastic properties [31] [32]. The RUS data was measured using the Magnaflux Quasar RUSpec system at the U.S. Army Research Laboratory in Aberdeen Proving Ground, Maryland. The sample is held in place between two transducers as the system sweeps frequencies, and the resonant frequencies of the sample appear as peaks in the measured spectrum. The samples' dimensions are measured by hand using a micrometer, while densities are measured using the Archimedes' method. This data is input into the RUSpec system as part of the sample information. Using the density, the dimensions and the resonant frequencies, the RUSpec software performs iterations using the Levenberg - Marquardt algorithm to generate a best fit to the resonant frequencies and thus determine the elastic constants of the sample and the wave speeds which can be found in Table 4.1.

3.3. *Microscale Computed Tomography (microCT)*

3.3.1. *MicroCT Scanning*

The pristine and thermally shocked samples were scanned with a Bruker Skyscan 1172 to determine crack characteristics. Scans were performed on the thermally cracked material as well as pristine material to determine a baseline level of damage. Each specimen was mounted on a flat brass spindle using a small foam substrate, and wrapped with parafilm to deter any slight movement during the scan. Single projection images were then examined to determine the proper sensor exposure time as well as tube current and voltage. These were found to be 149 μA and 29 kV with an exposure time of $2,500$ ms. A pixel size of 1.34 μm was used to obtain highest resolution of crack morphology while maintaining a reasonable scan time. The scanning results in approximately $2,000$ to $4,000$ projection images per specimen depending on the orientation of the sample.

3.3.2. 3D Reconstruction

The images obtained from CT are then processed to build up a 3D reconstruction of the fractures within the samples. Processing is performed first on the series of 2D images from the scans before a 3D model of the crack morphology can be built. Fig. 3 shows the processing procedure for each projection image. The features shown are internal as each projection image corresponds to a cross-section with a different depth in the specimen. We have not shown pristine sample scans for brevity, but they resemble the image seen in Fig. 3a and have similar bright spots corresponding to microstructural features, but lack any visible lines corresponding to internal fracture.

The region of interest (ROI) for image processing is defined manually to be close to, but within, the boundary of the material to prevent the edges of the sample from being construed as cracks due to the high contrast at the perimeter. This is done by clicking on points within the image through custom software to create a convex polygon whose lines do not intersect with the boundary of the specimen in the scan. Note that the region of interest shifts slightly from image to image, and so a ROI is defined for the first and last images and a linear interpolation is used between the two limits.

In the initial image, the background material is gray with cracks making bright lines on the image. The pixels corresponding to the bright lines of the cracks only make up a small percentage of the image. Background removal (Fig. 3b) is applied whereby for every pixel the mean intensity value for the neighborhood of pixels around it is subtracted from its intensity. This produces a new image with lower intensity than the original image at every pixel. As the bright cracks never make up a significant portion of a neighborhood by percentage of pixels, the resulting image contains low intensity (black) pixels where background (gray) pixels previously existed. Although the bright pixels are not as bright as they were before, they stand out more against the now darker background pixels which have almost zero intensity as can be seen in in Fig. 3b. Simple contrast adjustment of this background image brings the initially bright pixels back up to a high intensity (Fig. 3e). Although this also makes background noise brighter as well, by thresholding most of this can be removed and this results in the binary image in Fig. 3f.

In addition to contrast adjustment, gradient imaging enhances sharp contrasts at the sides of cracks. Median filtering is used to reduce some of the noise introduced by the gradient imaging resulting in Fig. 3c. This image is also converted to a binary images with simple thresholding based of a percentile value of the intensity values for the whole ROI. As each of the two processing paths described above has a tendency to miss a few features, the resulting binary images are combined to create a final image.

A stack of K binary images output from the 2D processing, each $M \times N$, results in a binary 3D matrix of size $K \times M \times N$. This initial matrix poses the difficulties of (i) large amounts of noise, which appear as pixelized white features in 2D, and (ii) computational difficulties due to the number of indices (i.e., size of the data). A scan for a single specimen can contain $\approx 2,500$ images with each image being $\approx 4,000 \times 4,000$ pixels. The corresponding 3D matrix would have $40,000,000,000$ indices or voxels (volume-pixels) at full resolution.

These difficulties are overcome by scaling down the binary matrix to a new integer

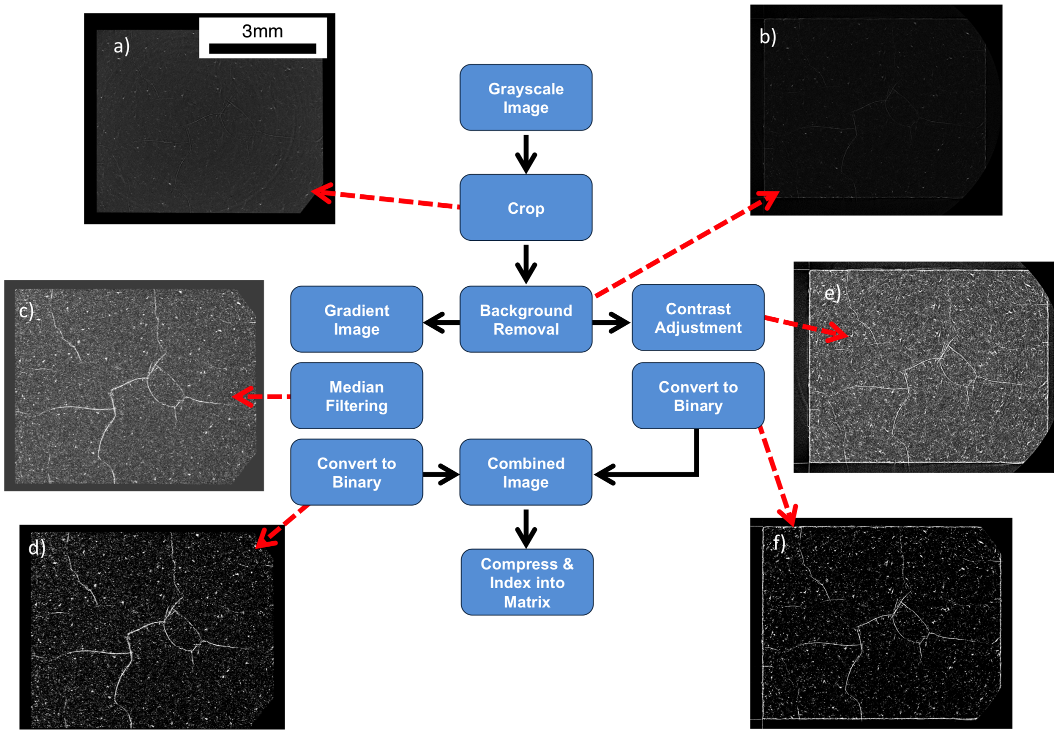

Fig. 3: Image processing flowchart for 2D input image. a) Cropped image with cropping defined within a few microns of the material boundary (see next figure for original image). b) Image after applying a background removal algorithm c) Result of applying median filtering to the gradient image of the result of the background removal step. d) Thresholded binary image from median filtering results e) Contrast adjusted version of background removed image f) Thresholded binary image from contrast adjusted image

matrix. For an initial binary matrix $\mathbf{B}$ of size $K \times M \times N$ a new integer matrix, $\mathbf{S}$ of size $\frac{K}{f} \times \frac{M}{f} \times \frac{N}{f}$ where f is an integer value that defines the scale parameter. For a set of indices (i, j, k) we define $p_i = f(i-1)+1$, $q_j = f(j-1)+1$, and $r_k = f(k-1)+1$. The large binary matrix $\mathbf{B}$ is then mapped to the integer matrix $\mathbf{S}$ as

$$\mathbf{S}(i, j, k) = \sum_{p=p_i}^{fi} \sum_{q=q_j}^{fj} \sum_{r=r_k}^{fk} \mathbf{B}(p, q, r) \tag{1}$$

The entries in the new matrix $\mathbf{S}$ are in the range of 0 to f^3. In the resulting integer matrix regions that correspond to cracks then contain a high integer value whereas regions of noise or microstructural defects contain low integer values. A threshold value, v is defined where $0 < v < f^3$ to obtain a final binary matrix, $\mathbf{M}$ from $\mathbf{S}$.

$$\mathbf{M}(i, j, k) = \begin{cases} 1, & \text{if } \mathbf{S}(i, j, k) > v \\ 0, & \text{otherwise} \end{cases} \tag{2}$$

By thresholding this integer matrix, noise regions where $0 < \mathbf{S}(i, j, k) < v$ can be removed resulting in a binary 3D matrix whose non-zero entries correspond to crack locations. The degree to which the initial matrix should be scaled down and the proper thresholding value would depend on the degree of noise in the initial image and how wide (in terms of pixels) cracks appear. In our case a scale value of $f = 6$ was found to provide good results while also greatly reducing computation time. This reduces the number of matrix entries from ≈ 40 billion to ≈ 185 million.

Two different approaches were used to generate 3D STL (Stereolithography) file representations from this binary matrix, $\mathbf{M}$. An STL file simply contains a list of vertices and a list of triangular faces comprised of these vertices. A series of connected triangular faces is referred to as a "mesh." An STL mesh can either be "two-manifold" or "non-manifold." Simply put, a two-manifold mesh could be split along edges and laid flat without any faces overlapping. A non-manifold mesh will contain features such as "T" junctions where three or more triangular faces share an edge, faces that share vertices but not edges, adjacent faces with opposite normals, or other non-manifold features [33]. When creating a 3D file to represent a fracture surface it may be ideal to represent it as a zero-thickness surface as cracks are not typically considered to have a volume. However, representing any sufficiently complex crack network as a zero thickness surface necessitates creating it as a non-manifold mesh as intersecting fracture surfaces will create "T" junctions or non-consistent surface normals.

Two reconstruction techniques were pursued. The first method will be referred to as a manifold "volume method" as it creates a manifold mesh where all fracture surfaces have 2 sides and therefor an enclosed volume. The second method will be referred to as a "surface method" as it creates a zero-thickness surface though a non-manifold mesh.

3.3.3. Volume Approach

The volume method produces a finite thickness surface to represent the crack structure. A penny shaped crack, for example, would be represented as an ellipsoid with this approach. In order to give the cracks two sides, the indices where $\mathbf{M}(i, j, k) = 1$ are padded with 1s in all direction to make the cracks thicker resulting in the matrix $\mathbf{M}'$. After this, the resulting matrix is smoothed using a Gaussian smoothing algorithm. With the cracks thickened, a Marching Cubes (MC) algorithm is used to turn the voxel matrix $\mathbf{M}'$ into a triangulated surface. A detailed explanation of the MC algorithm is contained in the references [34]. The complexity of the resulting mesh is then reduced using a Quadric Edge Collapse decimation algorithm. Finally, the resulting surface is smoothed out using a Poisson surface reconstruction. Renderings of the resulting 3D file can be seen in Fig. 4.

3.3.4. Surface Approach

The surface method approach produces a zero-thickness surface to represent the crack structure. The final binary matrix, $\mathbf{M}$ is converted to a point cloud, which is a list of XYZ coordinates corresponding to locations of 1s in the matrix. Once a point cloud has been created, the complexity of the point cloud is reduced using a clustered vertex subsampling approach. After this, a local surface normal can be approximated on a per point basis based on the location of nearby points. Once a point cloud with defined point normals has been constructed a 3D Stereolithography file containing a list of faces and vertices can be created. As crack intersections are more feasibly characterized with a zero-thickness surface representation, a segmentation algorithm was developed to segment the branched fracture network into individual surfaces.

3.3.5. 3D Segmentation

The segmentation of separate cracks from the connected crack network is an unresolved challenge in the literature and an on-going research topic in the authors' groups. A segmentation algorithm was developed to divide the zero-thickness surface described above into a set of disjoint, approximately planar surfaces. Segmentation begins by removing mesh faces that are expected to branch different crack surfaces. First, a curvature parameter is defined over the whole crack surface on a per face basis. Faces with a curvature value that is above a computed threshold are likely located at the junction between two crack surfaces and are therefor removed. After removing this initial set of faces, all faces that share an edge with only two or fewer faces are removed. A breadth-first search (BFS) is then run over the set of remaining faces. This approach considers faces to be individual graph nodes whereby two nodes are adjacent if their corresponding mesh faces share an edge. The BFS generates a spanning forest containing spanning trees where each spanning tree contains the set of faces that comprise an individual crack. For large crack faces further segmentation is performed using face normal parameter that splits large, curved, crack surfaces into smaller groups with more consistent face normals.

3.4. Mechanical Testing

3.4.1. Quasistatic Testing

Quasistatic compression tests were performed on an MTS Model C43.504 load frame fitted with MTS Model LPS.504 load cells with a maximum load capacity of

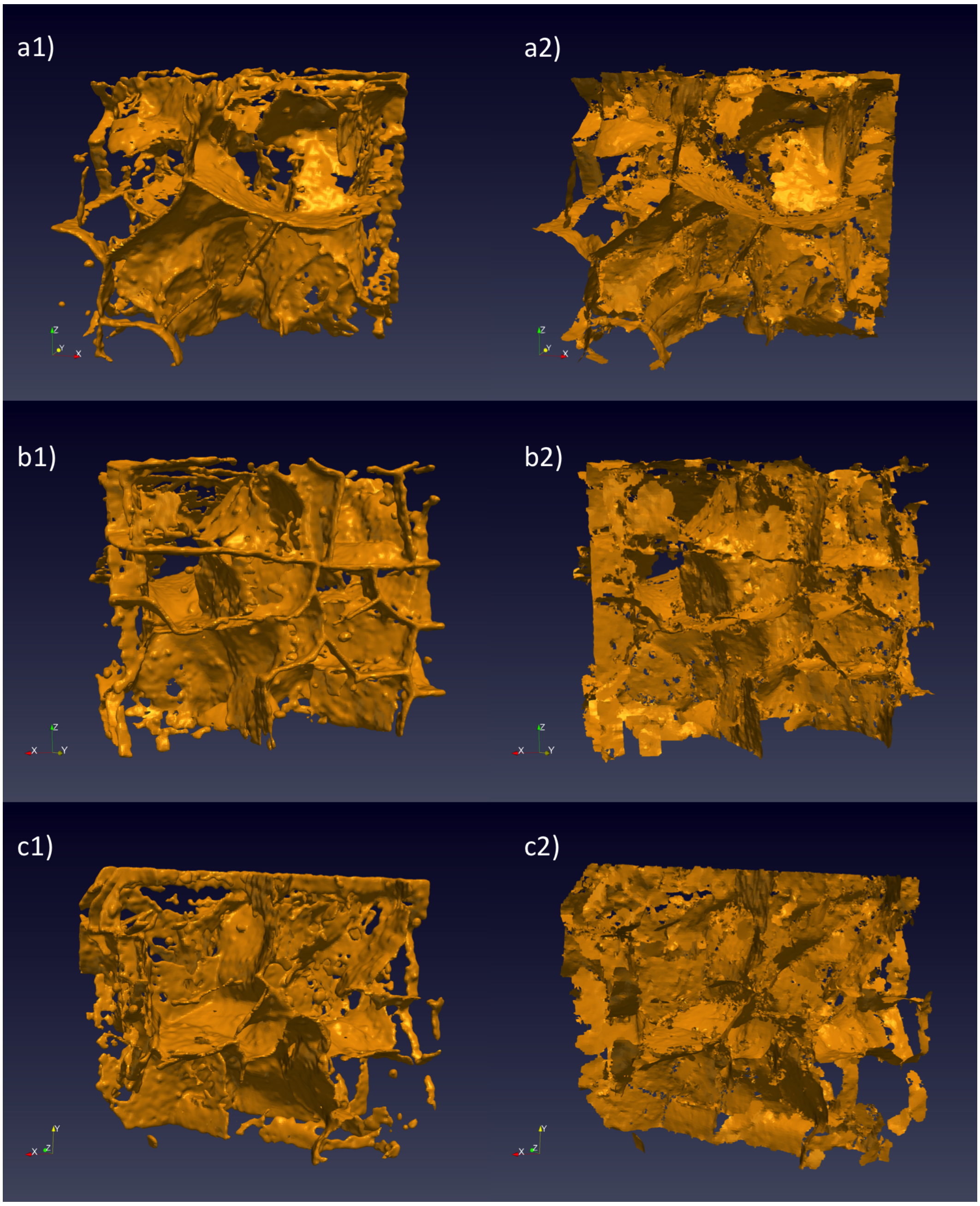

Fig. 4: 3 views of the reconstructions for sample TC69 are shown. The z-axis is the scan direction and the x-axis is the sintering (or TT) direction. The renderings on the left are from the volume reconstruction method (two-manifold). The renderings on the right are from the surface reconstruction (non-manifold). The length in the z-direction is approximately 3.2 mm

50 kN. As the boron carbide is harder than the hardened steel platens of the MTS machine, intermediate platens machined from SiC-N or WC with cross-sectional areas larger than that of the boron carbide specimens were used to transmit the compressive load to the boron carbide specimen without damaging the steel platens. A thin sleeve of plastic sheeting was wrapped loosely around the specimen and SiC-N platens to allow for collection of fragments after failure. Compression tests were run with a cross-head displacement rate of 5 μm/s, resulting in a nominal strain rate of $\approx 10^{-3}$ /s.

3.4.2. Dynamic Testing

Dynamic uniaxial compression was performed via a Kolsky bar apparatus. The Kolsky bar setup consists of an incident and transmitted bar that sandwich the specimen and a striker bar which impacts the incident bar propagating a stress pulse through it towards the specimen. Kolsky bars have been used extensively to study ceramics including boron carbide and details on experimental design can be readily found in literature [35].

The incident and transmitted bars, and projectile all had a diameter of 12.7 mm and are made of maraging steel (VascoMax C-350) with a yield strength of 2.68 GPa, elastic modulus of 200 GPa, Poisson's ratio of 0.29, and a density of $8,100$ kg/m^3. Their respective lengths were 1220 mm, 1050 mm and 127 mm. The length of the projectile dictates the width of the stress pulse transmitted through the bars. To protect against damaging the contact surface of the bars, 5 mm platens were placed on both sides of the sample at the interface with the incident and transmitted bars. Platens were made of impedance matched tungsten carbide (LC403, Leech Carbide) jacketed by Ti-6Al-4V sleeves. A small amount of grease was applied at both faces of each platen to reduce friction resulting from the differences in Poisson's ratio. Thin disks of copper and graphite were stacked on each other with a small amount of grease and placed on the impact end of the incident bar to improve the shape of the stress-pulse.

A Kirana highspeed camera was used to visualize one of the exposed faces of the cuboidal specimen for imaging the failure. Imaging was performed at a frame rate of 2 million frames per second with an exposure time of 500 ns. A diffuse class 4 laser and 2 flashbulbs were used to supply sufficient lighting for imaging. A strain gauge placed on the incident bar is used to trigger the camera with a fixed time offset that accounts for the wave speed in the bar to allow for imaging as the stress pulse loads the sample.

4. Results & Discussion

4.1. Characterization

A total of 7 samples were thermally shocked. CT and RUS were performed on 5 of these samples, as well as 3 pristine samples. No cracks are seen in the pristine sample although larger microstructural features can be seen. For all thermally shocked samples a full 3D file of the internal crack structure was constructed. Crack surface areas, wave speed measurements, and Poisson's ratio values from RUS are summarized in Table 4.1.

Sample	Thermal Cycling	Crack Area (mm^2)		Wavespeed (km/s)		ν
		Non-manifold	Two-manifold	Longitudinal	Shear	
TC69	2 Cycles, 850°C	75	57	13.99	8.75	0.179
TC71	1 Cycles, 550°C	28	21	13.88	8.71	0.176
TC72	2 Cycles, 750°C	54	43	13.84	8.72	0.171
TC73	1 Cycles, 750°C	41	33	13.81	8.72	0.169
TC76	2 Cycles, 650°C	40	31	14.02	8.70	0.187
TC52	none	-	-	13.90	8.61	0.189
TC55	none	-	-	13.95	8.61	0.192
TC56	none	-	-	13.80	8.63	0.179

Table II: Thermal history, crack area, wavespeed, and Poisson's ratio (ν) measurements for thermally shocked samples.

The average longitudinal wave speed value was 13.88 ± 0.08 km/s (intact) and 13.91 ± 0.09 km/s (damaged), the average shear wave speed was 8.62 ± 0.01km/s (intact) and 8.72 ± 0.02 km/s (damaged), the average Poisson's ratio was 0.187 ± 0.007 (intact) and 0.176 ± 0.007 (damaged). In summary, there is little to a slight increase in longitudinal wave speed, a notable increase in the shear wave, and notable decrease in the Poisson's ratio. The longitudinal wave speeds are slightly higher than the theoretical value 13.6 km/s [36] but close to the reported value experimentally found for sintered boron carbide 14.09 km/s [37]. In some scenarios damage is expected to decrease the longitudinal wave speed and Young's modulus [38]. The data presented here show no decrease in longitudinal wave speed for the damaged material, but rather show a slight increase that is well within the standard deviation of wave speeds seen for intact material and likely not statistically significant. Note that the material studied here has porosity derived for closed cracks at porosity levels of ~ 1 to 2%, whereas the majority of the literature deals with materials that have presumably near-spherical pore shapes. Previous studies on coal have also shown that microfractures do not necessarily decrease the velocity of elastic waves and may even lead to a slight increase [39]. Similar trends have been noted by Phani [40] in porcelain. Given that the Young's modulus and density are relatively unchanged by the introduction of pre-damage, the increase in shear wave speed may be a consequence of the decrease in Poisson's ratio given that they are related by

$$v_{shear} = \sqrt{\frac{E}{2(1+\nu)\rho}} \tag{3}$$

There are numerous papers that demonstrate a decrease in Poisson's ratio for increasing porosity [41] [42]. Yu et al. [41] also demonstrate that the ratio of longitudinal and shear wave speed decreases with increasing porosity (as our results indicate). The exact mechanism for these behaviors is outside the scope of this work but is likely related to the size, closure, and orientation of the cracks. In our study, the presence of pre-existing cracks is clearly shown in the CT reconstructions, it is possible that RUS may only be a good indicator of internal damage in advanced ceramics when initial damage levels are significantly higher than seen here.

Shown in Fig. 4 is a 3D surface reconstruction showing a branched crack network with cracks that seem to span the whole specimen. The reconstruction program developed for this work outputs STL files thats can be viewed in many commercial 3D visualization program (Blender, Meshlab, etc). The orange surfaces show the crack structure and empty space within this structure represents uncracked material. Many of the cracks intersect the sample boundary, consistent with the expectation that cracks will form at the boundary during thermal shock due to high local tensile stresses. It is also clear that straight crack segments are on a similar length scale to the entire specimen with cracks often being longer that 1 mm. Visual inspection of the left and right sides of Fig. 4 show that the two reconstruction algorithms result in very similar overall crack structures. The surface area values reported in Table 4.1 for the two-manifold surface is actually half the computed surface area as the cracks in this reconstruction have 2 sides. The crack area values in Table 4.1 show that the two-manifold approach consistently records a slightly lower crack area than the non-manifold surface. This is to be expected as the cracks in the non-manifold version often have greater extent than in the two-manifold version. This can be seen, for example, in the bottom right hand corner of Fig. 4c where the small floating crack is clearly larger in Fig. 4c2 than in Fig. 4c1.

As the crack structure is highly branched, reporting the number of cracks necessarily entails defining where one crack ends and another begins. This has implications for many microcrack based damage models which assume that cracks do not intersect. Although the number of cracks and their individual sizes may be difficult to report, it is easy to compute the surface area of all the resulting crack surfaces which may serve as a measure of the damage imparted to the sample. In addition to quantifying the extent of the cracking in terms of surface area, the orientation of crack faces can be characterized even if the crack structure is considered to be one continuous body instead of a group of discrete cracks. Understanding crack orientation is important as it governs how the cracks will interact with the stress field in the body under a specific loading direction [16].

4.2. Strength results & comparisons

Previous studies on this boron carbide tile have found a strength of 2.98 ± 0.60 GPa for the quasistatic case and 3.70 ± 0.30 GPa for the dynamic case for the through-thickness direction being tested here [5]. In the same vein, Fig. 5 and Fig. 6 below show a time-series comparison for the visualization of the failure of pristine and predamaged boron carbide with the same Kolsky bar setup.

For the intact specimen we see a spanning axial crack forming before the peak stress is achieved, followed by transverse cracking after the peak stress. For the damaged specimen large wing cracks can be seen on the photographed surface, likely emanating from cracks already in the the specimen, even before the peak stress is reached. Two notable features can be seen in the fracture and fragmentation of the damaged specimen when compared to the fragmentation of the intact specimen. First, we see large branching cracks spanning the specimen quickly and carving out large fragments during failure in damaged samples. Second, we see large fracture surfaces, likely from the initial crack

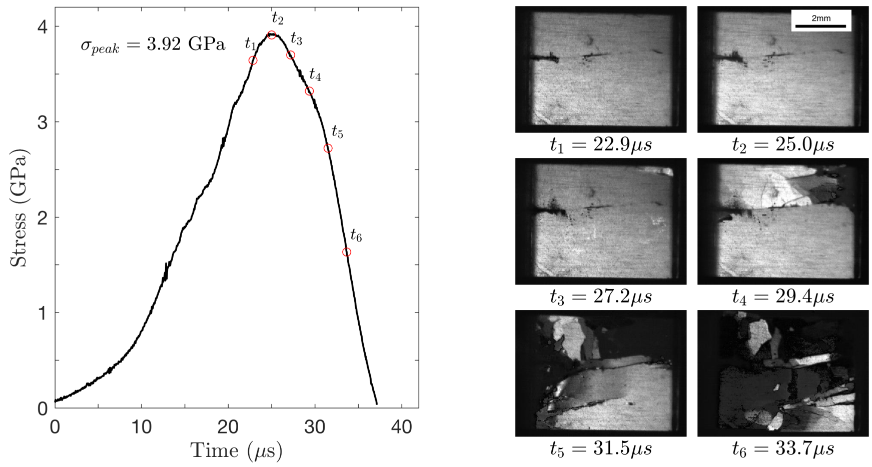

Fig. 5: Stress-time history of dynamic uniaxial compression of pristine boron carbide with time resolved high speed video images [4].

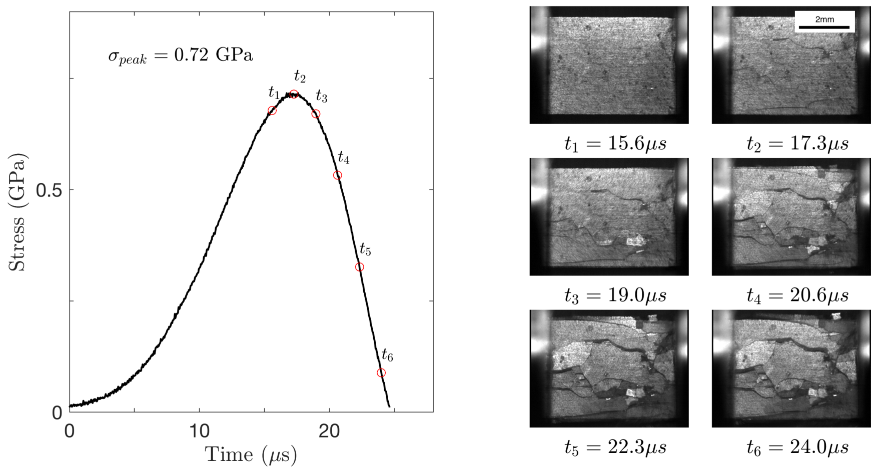

Fig. 6: Stress-time history of dynamic uniaxial compression of thermally damaged boron carbide with time resolved high speed video images. Note the difference in y-axis scale from the previous figure.

population on which frictional sliding is occurring. To the authors' knowledge, this is the first time that such failure observations for cracked materials have been made in the literature, and this could be important in models describing material failure. If the initial crack population serves as the initiation points for the generation of fragments, it may indicate that microstructure has a diminished role in the fragmentation of damaged material for the strain rates examined here.

The strength results for all quasistatic and dynamic tests from the damaged samples are summarized in Fig. 7. The peak strengths are in the range of 0.64 to 1.55 GPa across all rates. The x-axis gives the total crack area which we will consider now as a quantitative measure of the extent of initial cracking within the sample. In the figure, we plot the range of quasi-static strengths for the undamaged samples as red bars, and the range of dynamic strengths as blue bars with a dot showing the average value [5]. This is done for comparison purposes. Damaged samples are plotted as points, with red for quasi-static and blue for dynamic test results. For both dynamic and quasistatic tests, strength was significantly below what we would expect for intact material. It was also found that in general strength decreased with amount of predamage. This is to be expected as the stress intensity factor (SIF) should increase approximately with the size of the cracks. However, significantly more data are required to develop a direct quantitative relationship.

To discuss these results, we link with the work of Chocron et al. [1]. In that work, a thermal shock process at 750°C with 2 cycles was applied to boron carbide and the resulting strength of damaged material under confined compression and other multiaxial stress states was examined. The authors found that a Drucker-Prager yield law could be used to describe both damaged and intact material under confined compression. In the case of uniaxial compression with zero additional confining pressure, their model predicts a yield strength of 0.56 GPa for damaged material. For our samples under similar thermal cycling conditions we found a compressive strength of 0.64 GPa in the dynamic loading case and 0.87 to 1.01 GPa in the quasistatic case, which agrees reasonably well with the work of Chocron. Some scatter is to be expected due to the

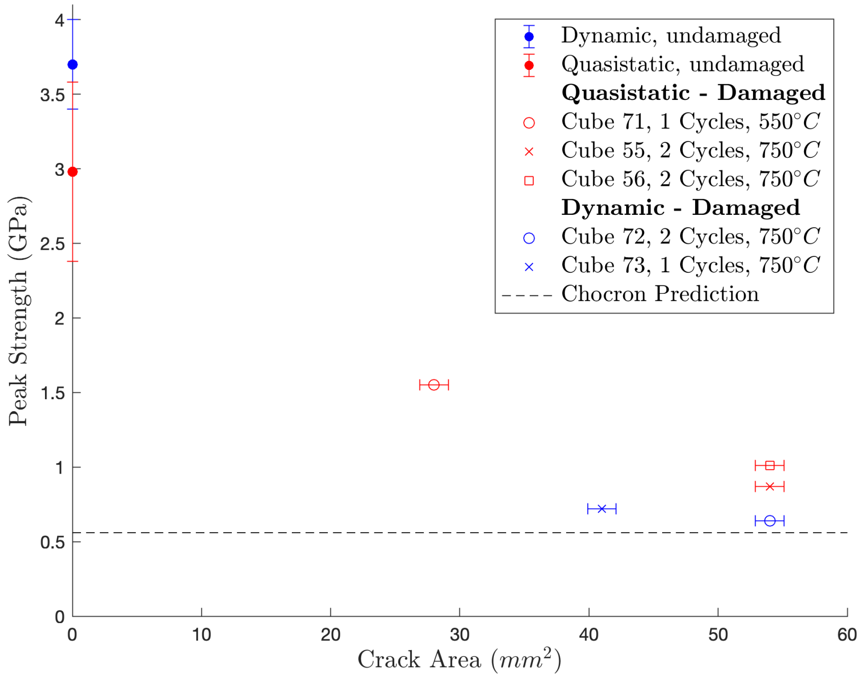

Fig. 7: Strength vs. crack area for quasistatic and dynamic tests on damaged material. The overlapping blue and red shaded regions show the ranges that would be expected for pristine material in the dynamic and quasistatic loading cases.

different specimen shape and size used which lead to different boundary conditions under thermal shock.

4.3. Rate effects discussion

Perhaps most surprising from the data presented here is the lower strength exhibited in the dynamic cases as compared to the quasistatic cases. Although small differences in results would be expected due to differences in test setup and inherent variability in testing ceramics, dynamic loading rates have generally been shown to increase the compressive strength of intact ceramics. However, strain rate does not appear to increase the strength of damaged ceramics, a result in agreement with Chocron et. al. [1].

The mechanics behind rate strengthening in ceramics has been well documented [29]. In short, crack growth can only dissipate energy at a finite rate dictated by the speed of elastic waves and crack tips in the material. When energy is input at a rate too high to be dissipated by growing pre-existing cracks or defects the additional energy goes into nucleating more cracks causing a rate strengthening effect. In the case of damaged material where there may be many large cracks already present in the material it is possible that a rate effect is still present but as there are already many available energy pathways, the transition strain rate above which a strong rate effect is seen might be significantly higher than it is for intact material. This, however, would not imply any reason for an inverse rate effect to be present in our samples. Ongoing work is required to confirm this result.

5. Conclusions

Samples of boron carbide were thermally damaged, characterized, and mechanically tested. Strength results for the damaged boron carbide are approximately in agreement with the only other available study on the strength of damaged boron carbide. A computational framework for creating a model of a 3D fracture network within a damaged material was developed and used to characterize the fracture network within 5 different specimens. The techniques developed here have the potential to be applied to a variety of other ceramic materials to study damage and crack growth. Future work will study damage evolution by repeatedly computing the crack structure after intermediate levels of damage have been applied.

6. Acknowledgments

This research was sponsored by the US Army Research Laboratory and was accomplished under Cooperative Agreement Number W911NF-12-2-0022. The views and conclusions contained in this document are those of the authors and should not be interpreted as representing the official policies, either expressed or implied, of the Army Research Laboratory or the U.S. Government. The U.S. Government is authorized to reproduce and distribute reprints for Government purposes notwithstanding any copyright notation herein. We acknowledge Michael Golt and Eric Warner for support of the RUS measurements. We thank Bryan Crawford of Johns Hopkins University as well as Matthew Shaeffer and Andrew Robinson of the Hopkins Extreme Materials Institute (HEMI) for helping run experiments. We also acknowledge Charles El Mir and Debjoy Mallick of HEMI for invaluable discussions throughout this project.

7. References

[1] Chocron S, Anderson Jr CE, Dannemann KA, Nicholls AE. Intact and Predamaged Boron Carbide Strength under Moderate Confinement Pressures. J Am Ceram Soc. 2012;95:350 – 357.

[2] Dannemann KA, Chocron S, Nicholls AE, Jr CEA. Compressive damage development in confined borosilicate glass. Material Science and Engineering: A. 2008;478(1-2):340 – 350.

[3] Elaqra H, Godin N, M R, Fantozzi G. Damage evolution analysis in mortar, during compressive loading using acoustic emission and X-ray tomography: Effects of the sand/cement ratio. Cement and Concrete Research. 2007;37(5):703 – 713.

[4] Hogan JD, Farbaniec L, Shaeffer M, Ramesh KT. The Effects of Microstructure and Confinement on the Compressive Fragmentation of an Advanced Ceramic. J Am Ceram Soc. 2014;p. 1 – 11.

[5] Hogan JD, Farbaniec L, Sano T, Shaeffer M, Ramesh KT. The effects of defects on the uniaxial compressive strength and failure of an advanced ceramic. Acta Materiala. 2016;102:263 – 272.

[6] Xie KY, Kuwelkar K, Haber RA, LaSalvia JC, Hemker KJ. Microstructural Characterization of a Commercial Hot-pressed Boron Carbide Armor Plate. J Am Ceram Soc. 2016;p. 1 – 8.

[7] Powell-Dogan CA, Heuer AH. Microstructure of 96AsâĂŘSintered Materials. J Am Ceram Soc. 1990;73(12):3670 – 3676.

[8] Farbaniec L, McCauley J, Hogan JD, Ramesh KT. Anisotropy of Mechanical Properties in a Hot-Pressed Boron Carbide. International Journal of Applied Ceramic Technology. 2016;p. 1 – 9.

[9] Ramesh KT, Hogan JD, Kimberley J, Stickle A. A review of mechanisms and models for dynamics failure, strength, and fragmentation. Planetary and Space Science. 2015;107:10 – 23.

[10] Ravichandran G, Subhash G. Critical Appraisal of Limiting Strain Rates for Compression Testing of Ceramics in a Split Hopkinson Pressure Bar. J Am Ceram Soc. 1994;77(1):263 – 267.

[11] Chen W, Ravichandran G. Dynamic compressive failure of a glass ceramic under lateral confinement. JMPS. 1997;45(8):1303 – 1328.

[12] Lankford J. Mechanisms Responsible for Strain-Rate-Dependent Compressive Strength in Ceramic Materials. J Am Ceram Soc. 1981;64(2):C–33 – C–34.

[13] Holland CC, McMeeking RM. The influence of mechanical and microstructural properties on the rate-dependent fracture strength of ceramics in uniaxial compression. International Journal of Impact Engineering. 2015;81:34 – 49.

[14] Deshpande VS, Evans AG. Inelastic deformation and energy dissipation in ceramics: A mechanism-based constitutive model. JMPS. 2008;56(10):3077 – 3100.

[15] Paliwal B, Ramesh KT. An interacting micro-crack damage model for failure of brittle materials under compression. JMPS. 2008;56:896 – 923.

[16] Hu G, Liu J, Graham-Brady L, Ramesh KT. A 3D Mechanistic model for brittle materials containing evolving flaw distributions under dynamic multiaxial loading. JMPS. 2015;78:269 – 297.

[17] Tonge AL, Kimberley J, Ramesh KT. A Consistent Scaling Framework for Simulating High Rate Brittle Failure Problems. Procedia Engineering. 2013;58:692–701.

[18] Johnson G, Holmquist TJ. Response of boron carbide subjected to large strains, high strain rates, and high pressures. Journal of Applied Physics. 1999;85(12):8060 – 8073.

[19] Tong AL, Ramesh KT. Multi-scale defect interactions in high-rate failure of brittle materials, Part II: Application to design of protection materials. Journal of the Mechanics and Physics of Solids. 2016;86:237 – 258.

[20] Nemat-Nasser S, Obata M. A Microcrack Model of Dilatancy in Brittle Materials. Journal of Applied Mechanics. 1988;55(1):24 – 35.

[21] Hogan JD, Farbaniec L, Mallick D, Domnich V, Kuwelkar K, Sano T, et al. Fragmentation of an advanced ceramic under ballistic impact: Mechanisms and microstructure. International Journal of Impact Engineering. 2016;102:47 – 54.

[22] Luo H, Chen W. Dynamic Compressive Response of Intact and Damaged AD995 Alumina. International Journal of Applied Ceramic Technology. 2004;1(3):254 – 260.

[23] Anderson Jr CE, Behner T, Orphal DL, Nicholls AE, Templeton DW. Time-resolved penetration into pre-damaged hot-pressed silicon carbide. International Journal of Impact Engineering. 2008;35(8):661 – 673.

[24] Shockey DA, Marchand AH, Skaggs SR, Cort GE, Burkett MW, Parker R. Failure phenomenology of confined ceramic targets and impacting rods. International Journal of Impact Engineering. 1990;9(3):263 – 275.

[25] Subhash G, Maiti S, Geubelle PH, Ghosh D. Recent Advances in Dynamic Indentation Fracture, Impact Damage and Fragmentation of Ceramics. Journal of the American Ceramic Society. 2008;91(9):2777 – 2791.

[26] Grady D. Impact failure and fragmentation properties of tungsten carbide. International Journal of Impact Engineering. 1999;23(1):307 – 317.

[27] Zinszner JL, Forquin P, Rossiquet G. Experimental and numerical analysis of the dynamic fragmentation in a SiC ceramic under impact. International Journal of Impact Engineering. 2015;76:9 – 19.

[28] Krell A, Strassburger E. Order of influences on the ballistic resistance of armor ceramics and single crystals. Materials Science & Engineering: A. 2014;597:422 – 430.

[29] Kimberley J, Hu G, Ramesh KT. A Scaled Model Describing the Rate-Dependent Compressive Failure of Brittle Materials. Dynamic Behavior of Materials. 2011;1:419 – 421.

[30] Hollenberg GW, Basmajian JA. Crack Propagation in Irradiated B4C Induced by Swelling and Thermal Gradients. J Am Ceram Soc. 1982;65(4):179 – 181.

[31] Migliori A, Sarrao J. Resonant ultrasound spectroscopy: application to physics, material measurement, and nondestructive evaluation. New York: Wiley; 1997.

[32] Migliori A, Darling T. Resonant ultrasound spectroscopy for materials studies and non-destructive testing. Ultrasonics. 1996;34(2-5):473 – 476.

[33] Autodesk Maya 2016 Documentation, Two-manifold and non-manifold polygonal geometry; 2016.

[34] Lorensen WE, Cline HE. Marching Cubes: A High Resolution 3D Surface Reconstruction Algorithm. Computer Graphics. 1987;21:163 –169.

[35] Chen WW, Song B. Split Hopkinson (Kolsky) Bar Design, Testing and Applications; 2011.

[36] Paliwal B, Ramesh KT. Effect of crack growth dynamics on the rate-sensitive behavior of hot-pressed boron carbide. Scripta Materiala. 2007;57:481 – 484.

[37] Brennan IV RE. (Dissertation), Ultrasonic Nondestructive Evaluation of Armor Ceramics; 2007.

[38] Damhof F, Brekelmans WAM, Geers MGD. Experimental analysis of the evolution of thermal shock damage using transit time measurement of ultrasonic waves. Journal of the European Ceramic Society. 2009;29(8):1309 – 1322.

[39] Shea VR, Hanson DR. Elastic Wave Velocity and Attenuation as Used to Define Phases of Loading and Failure in Coal. International Journal of Rock Mechanics and Mining Sciences & Geomechanics Abstracts. 1988;25(6):431 – 437.

[40] Phani KK. Correlation between ultrasonic shear wave velocity and Poisson's ratio for isotropic porous materials. Journal of Materials Science. 2007;43(1):316 – 323.

[41] Yu C, Ji S, Li Q. Effects of porosity on seismic velocities, elastic moduli and Poisson's ratios of solid materials and rocks. Journal of Rock Mechanics and Geotechnical Engineering. 2016;8(1):35 – 49.

[42] Asmani M, Kermel C, Leriche A, Ourak M. Influence of porosity on Young's modulus and Poisson's ratio in alumina ceramics. Journal of the European Ceramic Society. 2001;21(8):1081 – 1086.

- CT can be used to determine 3-dimensional crack structures in ceramics
- Internal cracks can lead to an increase in shear wave speed in ceramics
- Frictional sliding may be more likely to occur in pre-damaged ceramics
- Strain-rate strengthening effects may be diminished for cracked structures

Quantification of Damage and its Effects on the Compressive Strength of an Advanced Ceramic

Erez Krimsky[a,b], K.T. Ramesh[a,b], M. Bratcher[c], M. Foster[c], James David Hogan[d,*]

[a]*Hopkins Extreme Materials Institute, The Johns Hopkins University, Baltimore, MD 21218, USA*
[b]*Department of Mechanical Engineering, The Johns Hopkins University, Baltimore, MD 21218, USA*
[c]*U.S. Army Research Laboratory, Aberdeen Proving Ground, Maryland 21005, USA*
[d]*Department of Mechanical Engineering, The University of Alberta, Edmonton, AB T6G 2R3, Canada*

Abstract

An understanding of the dynamic failure of damaged ceramics is important in protection applications, where the interaction of the projectile with cracked material is a contributing factor in the overall system performance. In this paper, we investigate the effects of pre-existing internal cracks on the quasi-static and dynamic compressive behavior of an advanced ceramic. We present experiments on a hot-pressed boron carbide in which internal cracks are generated through thermal shocking after which the initial material damage is quantified. Damage characterization was performed via Resonant Ultrasound Spectroscopy (RUS) and high-resolution Computed Tomography (CT). A computational procedure is developed to determine the three-dimensional structure of the internal crack network in the initially damaged material from a series of CT images. The failure and strength of the material is then evaluated experimentally. The uniaxial compressive strength of the predamaged boron carbide samples is determined under both quasistatic and dynamic loading scenarios and this is correlated with the pre-existing crack structure as determined by CT. Damaged samples were found to have average compressive strength of 1.14 GPa in quasistatic loading and 0.68 GPa in dynamic loading compared to 2.98 ± 0.6 GPa and 3.70 ± 0.3 GPa for pristine material, respectively. High speed photography employed during dynamic testing indicates that pre-existing cracks may lead to different failure mechanisms from what is normally seen in pristine material. Ultimately, these insights can be used to design improved materials that are more resistant to dynamic failure.

Keywords: microcracks; thermal shock; compressive fragmentation; brittle failure; experimental mechanics; advanced ceramics;

---

*Corresponding Author
Email address: `jdhogan@ualberta.ca` (James David Hogan)

Nomenclature

$\mathbf{B}$	initial binary image matrix
E	elastic modulus
$\bar{l}$	average measured grain size
$\mathbf{M}$	final binary image matrix
$\mathbf{M}'$	padded final binary image matrix
$\bar{s}$	average defect size
$\mathbf{S}$	integer image matrix
v_{shear}	shear wave speed
η	defect density
ν	Poisson's ratio
ρ	density
μ_{log}	disk size lognormal distribution mean
μ_n	disk size normal distribution mean
σ_{log}	disk size lognormal distribution standard deviation
σ_n	disk size normal distribution standard deviation

1. Introduction

Designing advanced ceramics for protection applications requires an understanding of failure and fragmentation mechanisms. These mechanisms have been shown to depend on material processing and specifics of the stress-state and strain-rate. Recent work has aimed to understand how the presence of internal fractures prior to loading affects the failure process [1] [2] [3], and the results suggest that pre-existing cracks will have a considerable effect on the material response of advanced ceramics. Studying the mechanical response of damaged material will help us understand the process of damage evolution in advanced ceramics. This paper presents an approach to quantitatively measure the degree of damage within an advanced ceramic and then to relate this to its compressive response.

Previous studies of advanced ceramics have focused on characterizing the size, shapes, and types of microstructural features which are believed to serve as fracture initiation points [4] [5] [6] [7]. Studies have also focused on characterizing grain sizes and shapes, as well as material anisotropy [8]. Significant work has also been performed to characterize the rate-dependence of compressive strength [9] [10] [11] [12]. Under quasistatic compression the most deleterious defects are activated first, leading to crack growth and sample failure [5]. Under dynamic compression, however, the rate of loading is such that additional defects are activated before substantial crack growth occurs from the most deleterious defects (given finite crack speeds), and so dynamic loading leads to the activation of more distributed damage.

As experimental work has shown the importance of loading-rate, microstructural features, and microcracks in the failure process, computational models have been developed to try to capture these dependencies [13] [14]. The micro-mechanical modeling approach, for example, incorporates pre-existing flaw distributions in the material [15], and defines damage based on an evolving scalar crack density parameter. Similar work by Hu and Ramesh has further extended this type of model to account for flaw orientations and a tensorial damage parameter [16]. Tonge and Ramesh [17] further extended this approach into a full constitutive model with a computational implementation for large-scale simulations of impact events. Other researchers, such as Johnson and Holmquist, have modeled damage and damage evolution through a heuristic approach. The JH2 model defines a set of constants that can be determined by fitting experimental data over a wide range of loading conditions [18]. This approach does not directly incorporate any microstructure or crack statistics, yet can have strong predictive power when parameters are fit to a sufficiently large data set.

Motivated by the need to better understand the behavior of damaged materials and provide experimental data for modelling damaged behavior of brittle materials [18] [19] [20], this paper explores the quasistatic and dynamic compressive behavior of pre-cracked boron carbide. To accomplish damaged states, we thermally shock cuboidal specimens to produce internal crack networks that are ~mm in length scale and of the order of the test specimens. These crack networks are characterized through X-Ray tomography and Matlab-based image processing and are linked with mechanical properties and mechanical behavior. Other studies have used thermal shocking and mechanical loading to produce internal cracking in specimens within confined test setups [1] [2]. In this paper, we use thermal shocking because it allows us to produce porosities of interests (~ 1 to 3%) and crack sizes that are resolvable in X-Ray tomography scans, thus allowing, for the first time, a quantified measure of cracking that can be coupled to mechanical testing. The use of thermal shocking to produce ~ mm-sized cracked material also yields structural cracking sizes that are similar to those observed during impact into the same material [21], where understanding the impact behavior of this material is an overarching goal of this paper. In undertaking this research, attempts have been made to generate internal cracking through mechanical cycling, but this either resulted in too few and too small of cracks, or chipping at the specimen surface. Altogether, this work contributes to a limited data set in the literature for cracked specimens [1] [2] [22] [23], where the bulk of the work on advanced ceramics has focused on intact materials and resulting fragmentation [4] [21] [24] [25] [26] [27]. Understanding the behavior of materials for intermediate levels of damage is valuable in validating and improving models [16] [15] [17] [18] that can be used to design improved ceramic materials for, for example, ballistic impact, where fracture and fragmentation behaviors are important in their overall performance [28].

2. Material

The material in this study was a hot-pressed boron carbide (Coorstek, Inc.) with a Young's modulus of 430 GPa, a density of $2,510$ kg/m^3, a Poisson's ratio of 0.16 to 0.17, and a fracture toughness of 2.5 MPa $\sqrt{m}$. These values are provided by the manufacturer. The grain structure is equiaxed with an average grain size of 15 μm. Almost all the grain boundaries have a high misorientation angle (> 15°). This material has been used in previous studies by the authors and collaborators, where the focus has been on microstructural characterization [6], compressive strength and failure of intact forms [5] [8], compressive fragmentation [4], and impact fragmentation [21]. Additional details are provided in these references.

The boron carbide material was received as a tile (conceptualized in 1a with disk-like features in the figure meant to represent the carbonaceous inclusions presented later in b) with dimensions of 305 mm length, 254 mm in width, and 8 mm in thickness. For this study, rectangular prismatic boron carbide samples of approximate dimension $3.5 \times 4.0 \times 5.3$mm were machined from these larger tiles with the longest dimension being oriented along the hot-pressing or "through-thickness" (TT) direction. During sample machining, effort was made to minimize sub-surface damage by systematically polishing the edges from $\sim$ 100 μm finish to a 2 μm finish following the cutting operation. Examination of X-ray tomography scans (shown later) reveals no clear evidence of sub-surface damage from machining in the cubes under consideration in the current investigation.

The inclusions and defects in the microstructure were characterized using a Zeiss optical microscope with an AxioCam MRC camera and a TESCAN MIRA3 field emis-

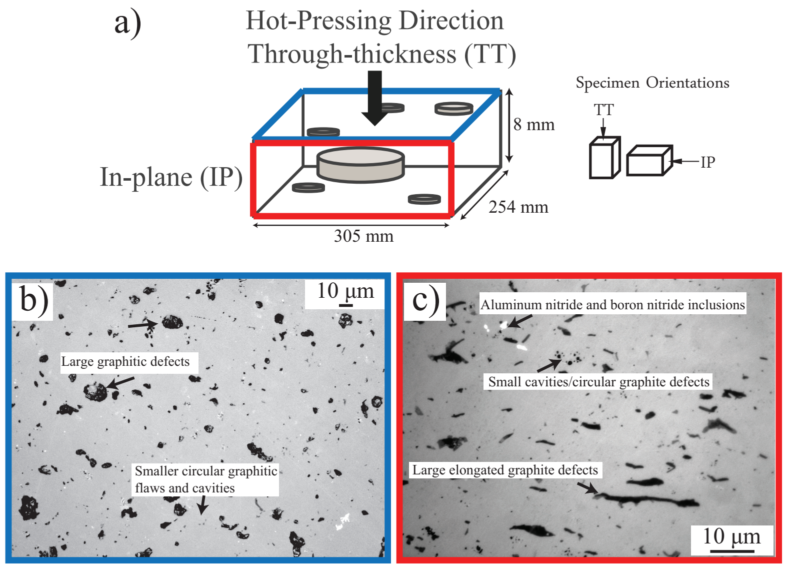

Fig. 1: (a) Conceptualized as-received tile of the hot-pressed boron carbide plate with through-thickness (TT) (in the hot-pressing direction) and in-plane directions (IP) labeled. Optical microscope images of the boron carbide microstructure in the (b) through-thickness (at 10 × magnification) and (c) in-plane direction (100× magnification) with the various types of inclusions and defects. [5]

sion Scanning Electron Microscope (SEM) equipped with a fully automated electron backscatter diffraction (EBSD) analysis system and Energy Dispersive Spectroscopy (EDS) capabilities. The word “defect” in this paper is used to denote a microstructural feature that may serve as a failure initiation site and “inclusion” is used to denote a feature that is not believed to contribute to failure (at least not under the stress states studied here). The processing-induced inclusions and defects are most easily seen in optical microscope images such as those shown in Fig. 1b and c. The image on the left is taken on the TT face, while the image on the right is taken on the IP face (note the different scale bars). Large, approximately circular, dark features are observed in the TT images in Fig. 1b. These have been confirmed to be carbonaceous in composition using EDS. Also highlighted in Fig. 1b are smaller and more circular features. These are primarily smaller graphitic defects, with other smaller features consisting of cavities/pores (confirmed with SEM/EDS). Brighter phases are also noted in Fig. 1b and these appear to be primarily comprised of aluminum nitride (AlN) and boron nitride (BN) (confirmed with SEM/EDS). These inclusions are faceted structures less than 20 μm in size, and are commonly observed at boron carbide grain boundaries.

Previous work has shown that graphitic disks in boron carbide are the microstructural features where fracture typically nucleates during failure in pristine (undamaged) specimens [5]. Again, these features are shown in the schematic representation of the as-received tile in Fig. 1a. The orientation, size, and spacing of these defects governs a variety of length scales that dictate rate dependence of the material strength [29]. These statistics are summarized in Table 2. The graphitic disk defect size was found to be well characterized by a lognormal distribution given by μ_{log} and σ_{log} whereas the defect orientation was found to be well characterized by a normal distribution given by μ_n and σ_n [5].

Material	$\bar{l}$ (μm)	η(#/m^2)	$\bar{s}$ (μm)	μ_{log} (μm)	σ_{log} (μm)	μ_n	σ_n
PAD Boron Carbide	16.0 ± 2.1	1.41×10^9	4.22 ± 2.54	1.30 ± 0.02	0.53 ± 0.02	0 ± 1°	20 ± 1°

Table I: Microstructure characteristics for pressure aided densification boron carbide, including $\bar{l}$: average measured grain size, η: defect density measured on the IP face for $s > 0.5\mu$m, $\bar{s}$: average defect size, μ_{log}, σ_{log}: disk size lognormal distribution parameters, μ_n, σ_n: disk orientation normal distribution parameters

For a material that already contains a significant number of flaws, it is not yet known exactly what effect the presence of these microstructure features will have upon the evolution of damage in a pre-damaged sample subjected to additional loading. We will explore this here.

3. Experimental Approach

Studies of damage evolution and the effects of internal cracking on the failure and strength of such materials [1] are limited. We use the approach described in Fig. 2 to capture the intermediate state of the material, with the intention of providing insight into dynamic damage evolution.

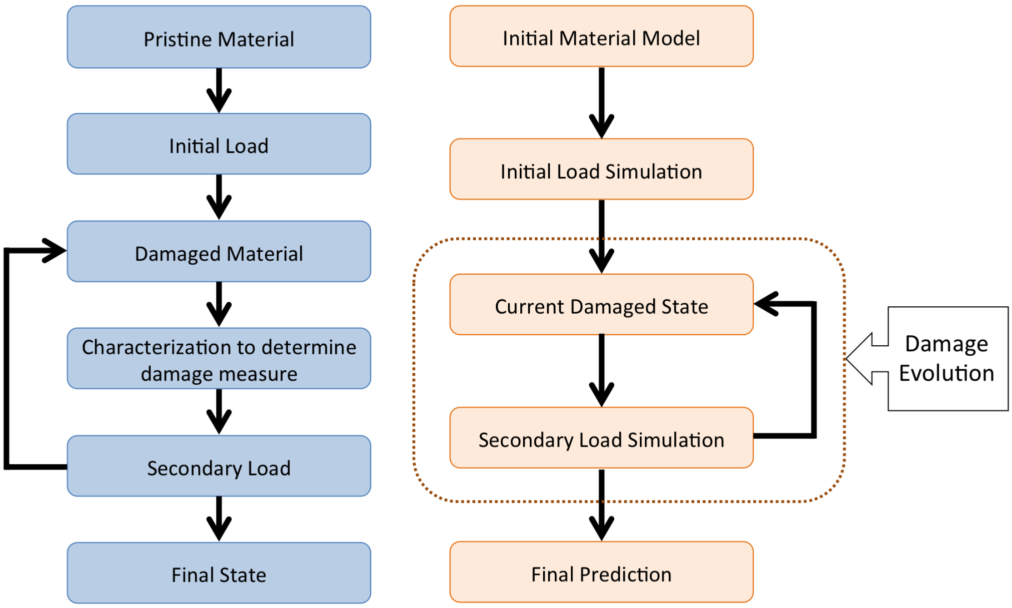

Fig. 2: Left: schematic showing the experimental process developed for this study. Traditional experiments go directly from the *initial load* to the *final state*. Right: schematic showing common computational procedure for simulating loading with damage evolution.

We achieve an intermediate damaged state by subjecting samples to an *initial load* that induces internal fracture without actually causing specimen fragmentation. The specimen is then characterized in this damaged state before an additional loading is provided. This process can be repeated until fragmentation occurs and the specimen has lost its load bearing capacity. The *pristine material* in our study is a sample of the boron carbide material described above. Although the specimen contains a variety of microstructural defects, it is considered to be free of damage until cracks have been induced by the initial (or primary) load. The *primary load* is performed via a thermal shock process described below. This leads to an intermediate *damaged material*. *Characterization* of this material provides a quantifiable *damage measure*. The characterization presented here was carried out via microscale CT to determine the internal crack structure and via resonant ultrasound spectroscopy to examine potential degradation of elastic properties. The secondary loading of this damaged sample is performed either via dynamic compressive testing with a Kolsky bar apparatus or through quasistatic compression with an MTS load frame system. The details of these tests are described below. If the secondary loading event does not fragment the sample, the process of characterization and loading can be repeated until a fragmented state is reached.

3.1. Thermal Shock

Material damage was induced via a thermal shock process. Previous studies on heated boron carbide with cooling on the boundary have shown that large thermal gradients lead to cracks propagating inward from the material boundary due to large tensile stresses [30]. For example, Chocron et. al. [1] investigated a thermal shock process through repeated heating and quenching on Pressure Assisted Densification (PAD) boron carbide and found that the extent of the crack propagation depends on the number of thermal cycles.

Five samples of boron carbide with approximate dimension $3.5 \times 4 \times 5.3$ mm were heated in a furnace in air. Samples were placed on small alumina tiles which could be easily manipulated with furnace tongs. The alumina tiles were placed on alumina foam blocks in the furnace. Samples were heated for ~ 1 hour to temperatures $550 - 850$°C. After heating, the alumina tiles were removed from the furnace and tipped over into a beaker of room temperature water thereby immersing the samples. Certain samples were run through two heat and quench cycles to increase the degree of internal cracking. The thermal cycling parameters of the samples can be found in Table 4.1. These are discussed later.

3.2. Resonant Ultrasound Spectroscopy

Pristine and thermally shocked samples were subjected to resonant ultrasound spectroscopy (RUS) to determine elastic properties [31] [32]. The RUS data was measured using the Magnaflux Quasar RUSpec system at the U.S. Army Research Laboratory in Aberdeen Proving Ground, Maryland. The sample is held in place between two transducers as the system sweeps frequencies, and the resonant frequencies of the sample appear as peaks in the measured spectrum. The samples' dimensions are measured by hand using a micrometer, while densities are measured using the Archimedes' method. This data is input into the RUSpec system as part of the sample information. Using the density, the dimensions and the resonant frequencies, the RUSpec software performs iterations using the Levenberg - Marquardt algorithm to generate a best fit to the resonant frequencies and thus determine the elastic constants of the sample and the wave speeds which can be found in Table 4.1.

3.3. Microscale Computed Tomography (microCT)

3.3.1. MicroCT Scanning

The pristine and thermally shocked samples were scanned with a Bruker Skyscan 1172 to determine crack characteristics. Scans were performed on the thermally cracked material as well as pristine material to determine a baseline level of damage. Each specimen was mounted on a flat brass spindle using a small foam substrate, and wrapped with parafilm to deter any slight movement during the scan. Single projection images were then examined to determine the proper sensor exposure time as well as tube current and voltage. These were found to be 149 μA and 29 kV with an exposure time of $2,500$ ms. A pixel size of 1.34 μm was used to obtain highest resolution of crack morphology while maintaining a reasonable scan time. The scanning results in approximately $2,000$ to $4,000$ projection images per specimen depending on the orientation of the sample.

3.3.2. 3D Reconstruction

The images obtained from CT are then processed to build up a 3D reconstruction of the fractures within the samples. Processing is performed first on the series of 2D images from the scans before a 3D model of the crack morphology can be built. Fig. 3 shows the processing procedure for each projection image. The features shown are internal as each projection image corresponds to a cross-section with a different depth in the specimen. We have not shown pristine sample scans for brevity, but they resemble the image seen in Fig. 3a and have similar bright spots corresponding to microstructural features, but lack any visible lines corresponding to internal fracture.

The region of interest (ROI) for image processing is defined manually to be close to, but within, the boundary of the material to prevent the edges of the sample from being construed as cracks due to the high contrast at the perimeter. This is done by clicking on points within the image through custom software to create a convex polygon whose lines do not intersect with the boundary of the specimen in the scan. Note that the region of interest shifts slightly from image to image, and so a ROI is defined for the first and last images and a linear interpolation is used between the two limits.

In the initial image, the background material is gray with cracks making bright lines on the image. The pixels corresponding to the bright lines of the cracks only make up a small percentage of the image. Background removal (Fig. 3b) is applied whereby for every pixel the mean intensity value for the neighborhood of pixels around it is subtracted from its intensity. This produces a new image with lower intensity than the original image at every pixel. As the bright cracks never make up a significant portion of a neighborhood by percentage of pixels, the resulting image contains low intensity (black) pixels where background (gray) pixels previously existed. Although the bright pixels are not as bright as they were before, they stand out more against the now darker background pixels which have almost zero intensity as can be seen in in Fig. 3b. Simple contrast adjustment of this background image brings the initially bright pixels back up to a high intensity (Fig. 3e). Although this also makes background noise brighter as well, by thresholding most of this can be removed and this results in the binary image in Fig. 3f.

In addition to contrast adjustment, gradient imaging enhances sharp contrasts at the sides of cracks. Median filtering is used to reduce some of the noise introduced by the gradient imaging resulting in Fig. 3c. This image is also converted to a binary images with simple thresholding based of a percentile value of the intensity values for the whole ROI. As each of the two processing paths described above has a tendency to miss a few features, the resulting binary images are combined to create a final image.

A stack of K binary images output from the 2D processing, each $M \times N$, results in a binary 3D matrix of size $K \times M \times N$. This initial matrix poses the difficulties of (i) large amounts of noise, which appear as pixelized white features in 2D, and (ii) computational difficulties due to the number of indices (i.e., size of the data). A scan for a single specimen can contain $\approx 2,500$ images with each image being $\approx 4,000 \times 4,000$ pixels. The corresponding 3D matrix would have $40,000,000,000$ indices or voxels (volume-pixels) at full resolution.

These difficulties are overcome by scaling down the binary matrix to a new integer

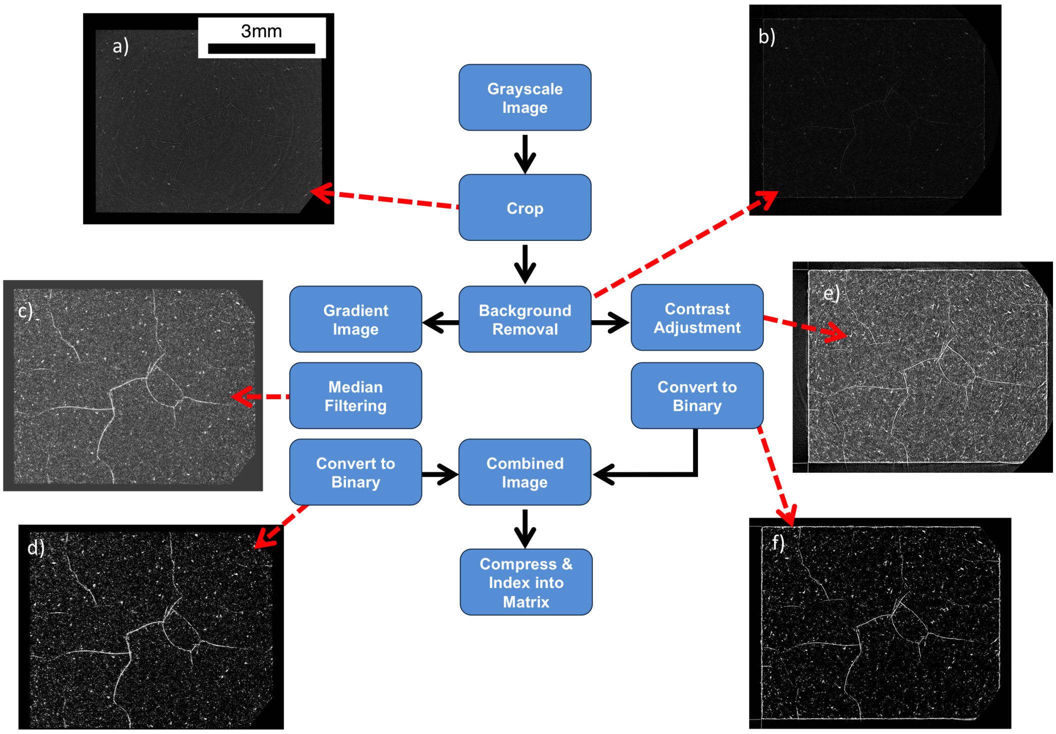

Fig. 3: Image processing flowchart for 2D input image. a) Cropped image with cropping defined within a few microns of the material boundary (see next figure for original image). b) Image after applying a background removal algorithm c) Result of applying median filtering to the gradient image of the result of the background removal step. d) Thresholded binary image from median filtering results e) Contrast adjusted version of background removed image f) Thresholded binary image from contrast adjusted image

matrix. For an initial binary matrix $\mathbf{B}$ of size $K \times M \times N$ a new integer matrix, $\mathbf{S}$ of size $\frac{K}{f} \times \frac{M}{f} \times \frac{N}{f}$ where f is an integer value that defines the scale parameter. For a set of indices (i, j, k) we define $p_i = f(i-1)+1$, $q_j = f(j-1)+1$, and $r_k = f(k-1)+1$. The large binary matrix $\mathbf{B}$ is then mapped to the integer matrix $\mathbf{S}$ as

$$\mathbf{S}(i, j, k) = \sum_{p=p_i}^{fi} \sum_{q=q_j}^{fj} \sum_{r=r_k}^{fk} \mathbf{B}(p, q, r) \tag{1}$$

The entries in the new matrix $\mathbf{S}$ are in the range of 0 to f^3. In the resulting integer matrix regions that correspond to cracks then contain a high integer value whereas regions of noise or microstructural defects contain low integer values. A threshold value, v is defined where $0 < v < f^3$ to obtain a final binary matrix, $\mathbf{M}$ from $\mathbf{S}$.

$$\mathbf{M}(i,j,k) = \begin{cases} 1, & \text{if } \mathbf{S}(i,j,k) > v \\ 0, & \text{otherwise} \end{cases} \tag{2}$$

By thresholding this integer matrix, noise regions where $0 < \mathbf{S}(i,j,k) < v$ can be removed resulting in a binary 3D matrix whose non-zero entries correspond to crack locations. The degree to which the initial matrix should be scaled down and the proper thresholding value would depend on the degree of noise in the initial image and how wide (in terms of pixels) cracks appear. In our case a scale value of $f = 6$ was found to provide good results while also greatly reducing computation time. This reduces the number of matrix entries from ≈ 40 billion to ≈ 185 million.

Two different approaches were used to generate 3D STL (Stereolithography) file representations from this binary matrix, $\mathbf{M}$. An STL file simply contains a list of vertices and a list of triangular faces comprised of these vertices. A series of connected triangular faces is referred to as a "mesh." An STL mesh can either be "two-manifold" or "non-manifold." Simply put, a two-manifold mesh could be split along edges and laid flat without any faces overlapping. A non-manifold mesh will contain features such as "T" junctions where three or more triangular faces share an edge, faces that share vertices but not edges, adjacent faces with opposite normals, or other non-manifold features [33]. When creating a 3D file to represent a fracture surface it may be ideal to represent it as a zero-thickness surface as cracks are not typically considered to have a volume. However, representing any sufficiently complex crack network as a zero thickness surface necessitates creating it as a non-manifold mesh as intersecting fracture surfaces will create "T" junctions or non-consistent surface normals.

Two reconstruction techniques were pursued. The first method will be referred to as a manifold “volume method” as it creates a manifold mesh where all fracture surfaces have 2 sides and therefor an enclosed volume. The second method will be referred to as a “surface method” as it creates a zero-thickness surface though a non-manifold mesh.

3.3.3. Volume Approach

The volume method produces a finite thickness surface to represent the crack structure. A penny shaped crack, for example, would be represented as an ellipsoid with this approach. In order to give the cracks two sides, the indices where $\mathbf{M}(i, j, k) = 1$ are padded with 1s in all direction to make the cracks thicker resulting in the matrix $\mathbf{M}'$. After this, the resulting matrix is smoothed using a Gaussian smoothing algorithm. With the cracks thickened, a Marching Cubes (MC) algorithm is used to turn the voxel matrix $\mathbf{M}'$ into a triangulated surface. A detailed explanation of the MC algorithm is contained in the references [34]. The complexity of the resulting mesh is then reduced using a Quadric Edge Collapse decimation algorithm. Finally, the resulting surface is smoothed out using a Poisson surface reconstruction. Renderings of the resulting 3D file can be seen in Fig. 4.

3.3.4. Surface Approach

The surface method approach produces a zero-thickness surface to represent the crack structure. The final binary matrix, $\mathbf{M}$ is converted to a point cloud, which is a list of XYZ coordinates corresponding to locations of 1s in the matrix. Once a point cloud has been created, the complexity of the point cloud is reduced using a clustered vertex subsampling approach. After this, a local surface normal can be approximated on a per point basis based on the location of nearby points. Once a point cloud with defined point normals has been constructed a 3D Stereolithography file containing a list of faces and vertices can be created. As crack intersections are more feasibly characterized with a zero-thickness surface representation, a segmentation algorithm was developed to segment the branched fracture network into individual surfaces.

3.3.5. 3D Segmentation

The segmentation of separate cracks from the connected crack network is an unresolved challenge in the literature and an on-going research topic in the authors' groups. A segmentation algorithm was developed to divide the zero-thickness surface described above into a set of disjoint, approximately planar surfaces. Segmentation begins by removing mesh faces that are expected to branch different crack surfaces. First, a curvature parameter is defined over the whole crack surface on a per face basis. Faces with a curvature value that is above a computed threshold are likely located at the junction between two crack surfaces and are therefor removed. After removing this initial set of faces, all faces that share an edge with only two or fewer faces are removed. A breadth-first search (BFS) is then run over the set of remaining faces. This approach considers faces to be individual graph nodes whereby two nodes are adjacent if their corresponding mesh faces share an edge. The BFS generates a spanning forest containing spanning trees where each spanning tree contains the set of faces that comprise an individual crack. For large crack faces further segmentation is performed using face normal parameter that splits large, curved, crack surfaces into smaller groups with more consistent face normals.

3.4. Mechanical Testing

3.4.1. Quasistatic Testing

Quasistatic compression tests were performed on an MTS Model C43.504 load frame fitted with MTS Model LPS.504 load cells with a maximum load capacity of

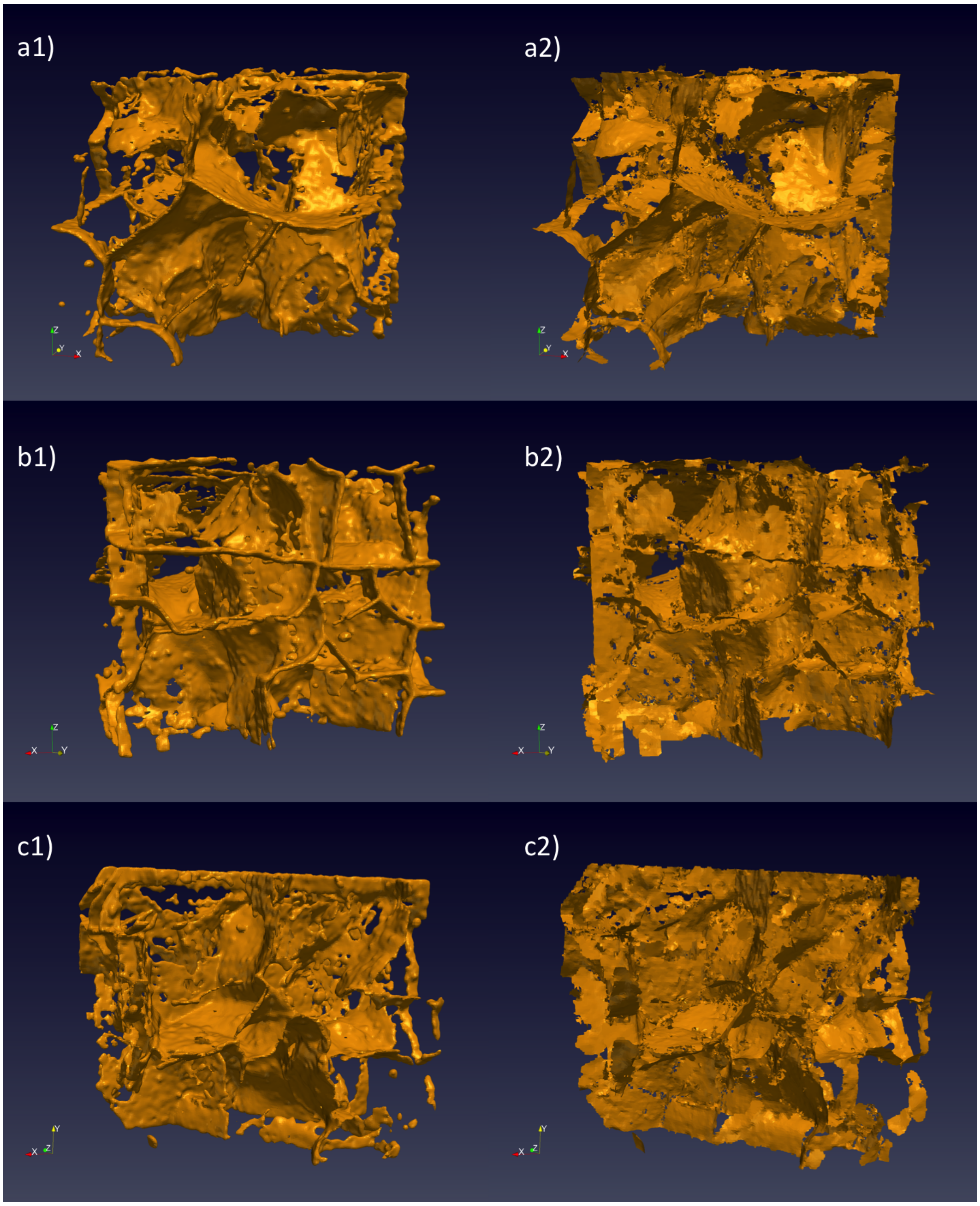

Fig. 4: 3 views of the reconstructions for sample TC69 are shown. The z-axis is the scan direction and the x-axis is the sintering (or TT) direction. The renderings on the left are from the volume reconstruction method (two-manifold). The renderings on the right are from the surface reconstruction (non-manifold). The length in the z-direction is approximately 3.2 mm

50 kN. As the boron carbide is harder than the hardened steel platens of the MTS machine, intermediate platens machined from SiC-N or WC with cross-sectional areas larger than that of the boron carbide specimens were used to transmit the compressive load to the boron carbide specimen without damaging the steel platens. A thin sleeve of plastic sheeting was wrapped loosely around the specimen and SiC-N platens to allow for collection of fragments after failure. Compression tests were run with a cross-head displacement rate of 5 μm/s, resulting in a nominal strain rate of $\approx 10^{-3}$ /s.

3.4.2. Dynamic Testing

Dynamic uniaxial compression was performed via a Kolsky bar apparatus. The Kolsky bar setup consists of an incident and transmitted bar that sandwich the specimen and a striker bar which impacts the incident bar propagating a stress pulse through it towards the specimen. Kolsky bars have been used extensively to study ceramics including boron carbide and details on experimental design can be readily found in literature [35].

The incident and transmitted bars, and projectile all had a diameter of 12.7 mm and are made of maraging steel (VascoMax C-350) with a yield strength of 2.68 GPa, elastic modulus of 200 GPa, Poisson's ratio of 0.29, and a density of $8,100$ kg/m^3. Their respective lengths were 1220 mm, 1050 mm and 127 mm. The length of the projectile dictates the width of the stress pulse transmitted through the bars. To protect against damaging the contact surface of the bars, 5 mm platens were placed on both sides of the sample at the interface with the incident and transmitted bars. Platens were made of impedance matched tungsten carbide (LC403, Leech Carbide) jacketed by Ti-6Al-4V sleeves. A small amount of grease was applied at both faces of each platen to reduce friction resulting from the differences in Poisson's ratio. Thin disks of copper and graphite were stacked on each other with a small amount of grease and placed on the impact end of the incident bar to improve the shape of the stress-pulse.

A Kirana highspeed camera was used to visualize one of the exposed faces of the cuboidal specimen for imaging the failure. Imaging was performed at a frame rate of 2 million frames per second with an exposure time of 500 ns. A diffuse class 4 laser and 2 flashbulbs were used to supply sufficient lighting for imaging. A strain gauge placed on the incident bar is used to trigger the camera with a fixed time offset that accounts for the wave speed in the bar to allow for imaging as the stress pulse loads the sample.

4. Results & Discussion

4.1. Characterization

A total of 7 samples were thermally shocked. CT and RUS were performed on 5 of these samples, as well as 3 pristine samples. No cracks are seen in the pristine sample although larger microstructural features can be seen. For all thermally shocked samples a full 3D file of the internal crack structure was constructed. Crack surface areas, wave speed measurements, and Poisson's ratio values from RUS are summarized in Table 4.1.

Sample	Thermal Cycling	Crack Area (mm^2)		Wavespeed (km/s)		ν
		Non-manifold	Two-manifold	Longitudinal	Shear	
TC69	2 Cycles, 850°C	75	57	13.99	8.75	0.179
TC71	1 Cycles, 550°C	28	21	13.88	8.71	0.176
TC72	2 Cycles, 750°C	54	43	13.84	8.72	0.171
TC73	1 Cycles, 750°C	41	33	13.81	8.72	0.169
TC76	2 Cycles, 650°C	40	31	14.02	8.70	0.187
TC52	none	-	-	13.90	8.61	0.189
TC55	none	-	-	13.95	8.61	0.192
TC56	none	-	-	13.80	8.63	0.179

Table II: Thermal history, crack area, wavespeed, and Poisson's ratio (ν) measurements for thermally shocked samples.

The average longitudinal wave speed value was 13.88 ± 0.08 km/s (intact) and 13.91 ± 0.09 km/s (damaged), the average shear wave speed was 8.62 ± 0.01km/s (intact) and 8.72 ± 0.02 km/s (damaged), the average Poisson's ratio was 0.187 ± 0.007 (intact) and 0.176 ± 0.007 (damaged). In summary, there is little to a slight increase in longitudinal wave speed, a notable increase in the shear wave, and notable decrease in the Poisson's ratio. The longitudinal wave speeds are slightly higher than the theoretical value 13.6 km/s [36] but close to the reported value experimentally found for sintered boron carbide 14.09 km/s [37]. In some scenarios damage is expected to decrease the longitudinal wave speed and Young's modulus [38]. The data presented here show no decrease in longitudinal wave speed for the damaged material, but rather show a slight increase that is well within the standard deviation of wave speeds seen for intact material and likely not statistically significant. Note that the material studied here has porosity derived for closed cracks at porosity levels of $\sim$ 1 to 2%, whereas the majority of the literature deals with materials that have presumably near-spherical pore shapes. Previous studies on coal have also shown that microfractures do not necessarily decrease the velocity of elastic waves and may even lead to a slight increase [39]. Similar trends have been noted by Phani [40] in porcelain. Given that the Young's modulus and density are relatively unchanged by the introduction of pre-damage, the increase in shear wave speed may be a consequence of the decrease in Poisson's ratio given that they are related by

$$\mathrm{v}_{shear} = \sqrt{\frac{E}{2(1+\nu)\rho}} \tag{3}$$

There are numerous papers that demonstrate a decrease in Poisson's ratio for increasing porosity [41] [42]. Yu et al. [41] also demonstrate that the ratio of longitudinal and shear wave speed decreases with increasing porosity (as our results indicate). The exact mechanism for these behaviors is outside the scope of this work but is likely related to the size, closure, and orientation of the cracks. In our study, the presence of pre-existing cracks is clearly shown in the CT reconstructions, it is possible that RUS may only be a good indicator of internal damage in advanced ceramics when initial damage levels are significantly higher than seen here.

Shown in Fig. 4 is a 3D surface reconstruction showing a branched crack network with cracks that seem to span the whole specimen. The reconstruction program developed for this work outputs STL files thats can be viewed in many commercial 3D visualization program (Blender, Meshlab, etc). The orange surfaces show the crack structure and empty space within this structure represents uncracked material. Many of the cracks intersect the sample boundary, consistent with the expectation that cracks will form at the boundary during thermal shock due to high local tensile stresses. It is also clear that straight crack segments are on a similar length scale to the entire specimen with cracks often being longer that 1 mm. Visual inspection of the left and right sides of Fig. 4 show that the two reconstruction algorithms result in very similar overall crack structures. The surface area values reported in Table 4.1 for the two-manifold surface is actually half the computed surface area as the cracks in this reconstruction have 2 sides. The crack area values in Table 4.1 show that the two-manifold approach consistently records a slightly lower crack area than the non-manifold surface. This is to be expected as the cracks in the non-manifold version often have greater extent than in the two-manifold version. This can be seen, for example, in the bottom right hand corner of Fig. 4c where the small floating crack is clearly larger in Fig. 4c2 than in Fig. 4c1.

As the crack structure is highly branched, reporting the number of cracks necessarily entails defining where one crack ends and another begins. This has implications for many microcrack based damage models which assume that cracks do not intersect. Although the number of cracks and their individual sizes may be difficult to report, it is easy to compute the surface area of all the resulting crack surfaces which may serve as a measure of the damage imparted to the sample. In addition to quantifying the extent of the cracking in terms of surface area, the orientation of crack faces can be characterized even if the crack structure is considered to be one continuous body instead of a group of discrete cracks. Understanding crack orientation is important as it governs how the cracks will interact with the stress field in the body under a specific loading direction [16].

4.2. Strength results & comparisons

Previous studies on this boron carbide tile have found a strength of 2.98 ± 0.60 GPa for the quasistatic case and 3.70 ± 0.30 GPa for the dynamic case for the through-thickness direction being tested here [5]. In the same vein, Fig. 5 and Fig. 6 below show a time-series comparison for the visualization of the failure of pristine and predamaged boron carbide with the same Kolsky bar setup.

For the intact specimen we see a spanning axial crack forming before the peak stress is achieved, followed by transverse cracking after the peak stress. For the damaged specimen large wing cracks can be seen on the photographed surface, likely emanating from cracks already in the the specimen, even before the peak stress is reached. Two notable features can be seen in the fracture and fragmentation of the damaged specimen when compared to the fragmentation of the intact specimen. First, we see large branching cracks spanning the specimen quickly and carving out large fragments during failure in damaged samples. Second, we see large fracture surfaces, likely from the initial crack

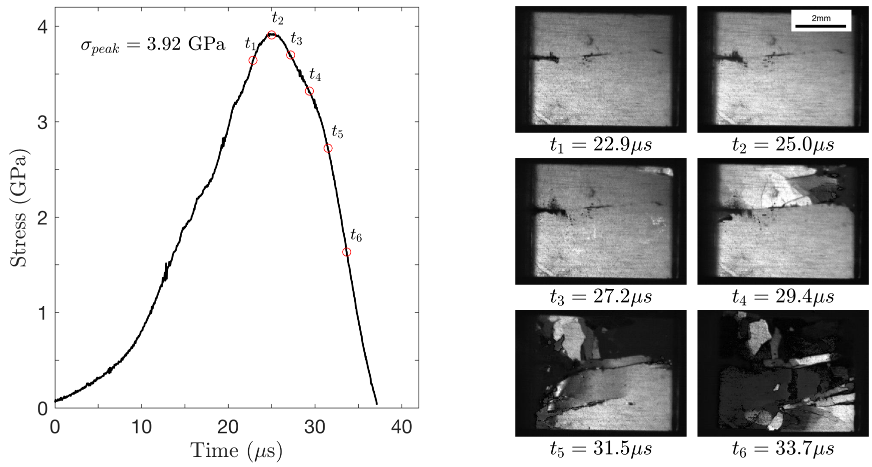

Fig. 5: Stress-time history of dynamic uniaxial compression of pristine boron carbide with time resolved high speed video images [4].

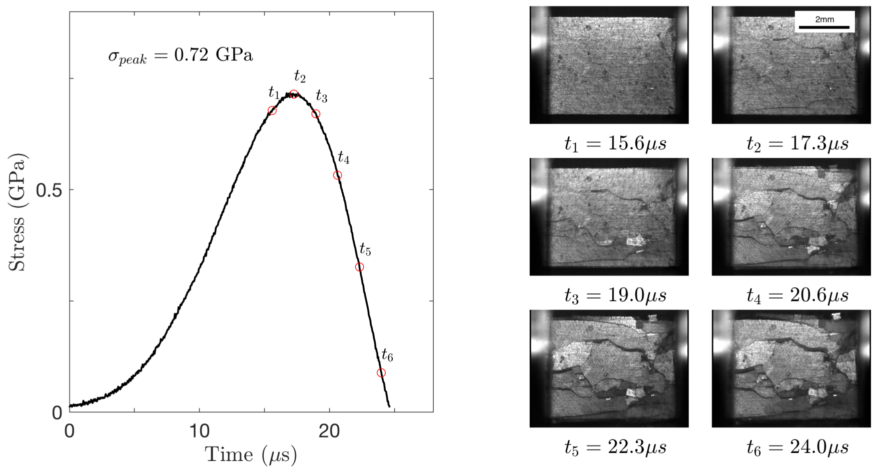

Fig. 6: Stress-time history of dynamic uniaxial compression of thermally damaged boron carbide with time resolved high speed video images. Note the difference in y-axis scale from the previous figure.

population on which frictional sliding is occurring. To the authors' knowledge, this is the first time that such failure observations for cracked materials have been made in the literature, and this could be important in models describing material failure. If the initial crack population serves as the initiation points for the generation of fragments, it may indicate that microstructure has a diminished role in the fragmentation of damaged material for the strain rates examined here.

The strength results for all quasistatic and dynamic tests from the damaged samples are summarized in Fig. 7. The peak strengths are in the range of 0.64 to 1.55 GPa across all rates. The x-axis gives the total crack area which we will consider now as a quantitative measure of the extent of initial cracking within the sample. In the figure, we plot the range of quasi-static strengths for the undamaged samples as red bars, and the range of dynamic strengths as blue bars with a dot showing the average value [5]. This is done for comparison purposes. Damaged samples are plotted as points, with red for quasi-static and blue for dynamic test results. For both dynamic and quasistatic tests, strength was significantly below what we would expect for intact material. It was also found that in general strength decreased with amount of predamage. This is to be expected as the stress intensity factor (SIF) should increase approximately with the size of the cracks. However, significantly more data are required to develop a direct quantitative relationship.

To discuss these results, we link with the work of Chocron et al. [1]. In that work, a thermal shock process at 750°C with 2 cycles was applied to boron carbide and the resulting strength of damaged material under confined compression and other multiaxial stress states was examined. The authors found that a Drucker-Prager yield law could be used to describe both damaged and intact material under confined compression. In the case of uniaxial compression with zero additional confining pressure, their model predicts a yield strength of 0.56 GPa for damaged material. For our samples under similar thermal cycling conditions we found a compressive strength of 0.64 GPa in the dynamic loading case and 0.87 to 1.01 GPa in the quasistatic case, which agrees reasonably well with the work of Chocron. Some scatter is to be expected due to the

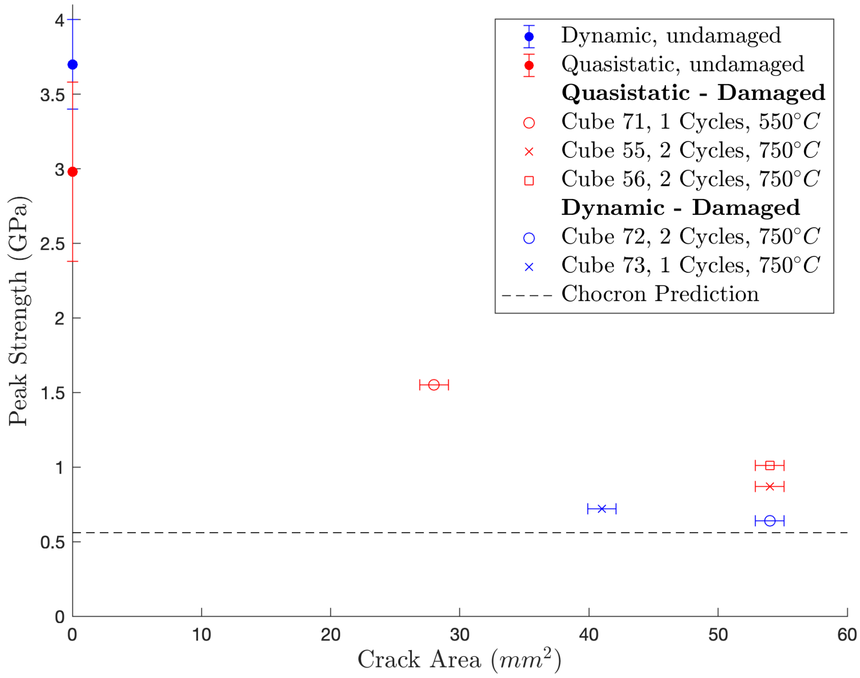

Fig. 7: Strength vs. crack area for quasistatic and dynamic tests on damaged material. The overlapping blue and red shaded regions show the ranges that would be expected for pristine material in the dynamic and quasistatic loading cases.

different specimen shape and size used which lead to different boundary conditions under thermal shock.

4.3. Rate effects discussion

Perhaps most surprising from the data presented here is the lower strength exhibited in the dynamic cases as compared to the quasistatic cases. Although small differences in results would be expected due to differences in test setup and inherent variability in testing ceramics, dynamic loading rates have generally been shown to increase the compressive strength of intact ceramics. However, strain rate does not appear to increase the strength of damaged ceramics, a result in agreement with Chocron et. al. [1].

The mechanics behind rate strengthening in ceramics has been well documented [29]. In short, crack growth can only dissipate energy at a finite rate dictated by the speed of elastic waves and crack tips in the material. When energy is input at a rate too high to be dissipated by growing pre-existing cracks or defects the additional energy goes into nucleating more cracks causing a rate strengthening effect. In the case of damaged material where there may be many large cracks already present in the material it is possible that a rate effect is still present but as there are already many available energy pathways, the transition strain rate above which a strong rate effect is seen might be significantly higher than it is for intact material. This, however, would not imply any reason for an inverse rate effect to be present in our samples. Ongoing work is required to confirm this result.

5. Conclusions

Samples of boron carbide were thermally damaged, characterized, and mechanically tested. Strength results for the damaged boron carbide are approximately in agreement with the only other available study on the strength of damaged boron carbide. A computational framework for creating a model of a 3D fracture network within a damaged material was developed and used to characterize the fracture network within 5 different specimens. The techniques developed here have the potential to be applied to a variety of other ceramic materials to study damage and crack growth. Future work will study damage evolution by repeatedly computing the crack structure after intermediate levels of damage have been applied.

6. Acknowledgments

This research was sponsored by the US Army Research Laboratory and was accomplished under Cooperative Agreement Number W911NF-12-2-0022. The views and conclusions contained in this document are those of the authors and should not be interpreted as representing the official policies, either expressed or implied, of the Army Research Laboratory or the U.S. Government. The U.S. Government is authorized to reproduce and distribute reprints for Government purposes notwithstanding any copyright notation herein. We acknowledge Michael Golt and Eric Warner for support of the RUS measurements. We thank Bryan Crawford of Johns Hopkins University as well as Matthew Shaeffer and Andrew Robinson of the Hopkins Extreme Materials Institute (HEMI) for helping run experiments. We also acknowledge Charles El Mir and Debjoy Mallick of HEMI for invaluable discussions throughout this project.

7. References

[1] Chocron S, Anderson Jr CE, Dannemann KA, Nicholls AE. Intact and Predamaged Boron Carbide Strength under Moderate Confinement Pressures. J Am Ceram Soc. 2012;95:350 – 357.

[2] Dannemann KA, Chocron S, Nicholls AE, Jr CEA. Compressive damage development in confined borosilicate glass. Material Science and Engineering: A. 2008;478(1-2):340 – 350.

[3] Elaqra H, Godin N, M R, Fantozzi G. Damage evolution analysis in mortar, during compressive loading using acoustic emission and X-ray tomography: Effects of the sand/cement ratio. Cement and Concrete Research. 2007;37(5):703 – 713.

[4] Hogan JD, Farbaniec L, Shaeffer M, Ramesh KT. The Effects of Microstructure and Confinement on the Compressive Fragmentation of an Advanced Ceramic. J Am Ceram Soc. 2014;p. 1 – 11.

[5] Hogan JD, Farbaniec L, Sano T, Shaeffer M, Ramesh KT. The effects of defects on the uniaxial compressive strength and failure of an advanced ceramic. Acta Materiala. 2016;102:263 – 272.

[6] Xie KY, Kuwelkar K, Haber RA, LaSalvia JC, Hemker KJ. Microstructural Characterization of a Commercial Hot-pressed Boron Carbide Armor Plate. J Am Ceram Soc. 2016;p. 1 – 8.

[7] Powell-Dogan CA, Heuer AH. Microstructure of 96AsâĂŘSintered Materials. J Am Ceram Soc. 1990;73(12):3670 – 3676.

[8] Farbaniec L, McCauley J, Hogan JD, Ramesh KT. Anisotropy of Mechanical Properties in a Hot-Pressed Boron Carbide. International Journal of Applied Ceramic Technology. 2016;p. 1 – 9.

[9] Ramesh KT, Hogan JD, Kimberley J, Stickle A. A review of mechanisms and models for dynamics failure, strength, and fragmentation. Planetary and Space Science. 2015;107:10 – 23.

[10] Ravichandran G, Subhash G. Critical Appraisal of Limiting Strain Rates for Compression Testing of Ceramics in a Split Hopkinson Pressure Bar. J Am Ceram Soc. 1994;77(1):263 – 267.

[11] Chen W, Ravichandran G. Dynamic compressive failure of a glass ceramic under lateral confinement. JMPS. 1997;45(8):1303 – 1328.

[12] Lankford J. Mechanisms Responsible for Strain-Rate-Dependent Compressive Strength in Ceramic Materials. J Am Ceram Soc. 1981;64(2):C–33 – C–34.

[13] Holland CC, McMeeking RM. The influence of mechanical and microstructural properties on the rate-dependent fracture strength of ceramics in uniaxial compression. International Journal of Impact Engineering. 2015;81:34 – 49.

[14] Deshpande VS, Evans AG. Inelastic deformation and energy dissipation in ceramics: A mechanism-based constitutive model. JMPS. 2008;56(10):3077 – 3100.

[15] Paliwal B, Ramesh KT. An interacting micro-crack damage model for failure of brittle materials under compression. JMPS. 2008;56:896 – 923.

[16] Hu G, Liu J, Graham-Brady L, Ramesh KT. A 3D Mechanistic model for brittle materials containing evolving flaw distributions under dynamic multiaxial loading. JMPS. 2015;78:269 – 297.

[17] Tonge AL, Kimberley J, Ramesh KT. A Consistent Scaling Framework for Simulating High Rate Brittle Failure Problems. Procedia Engineering. 2013;58:692–701.

[18] Johnson G, Holmquist TJ. Response of boron carbide subjected to large strains, high strain rates, and high pressures. Journal of Applied Physics. 1999;85(12):8060 – 8073.

[19] Tong AL, Ramesh KT. Multi-scale defect interactions in high-rate failure of brittle materials, Part II: Application to design of protection materials. Journal of the Mechanics and Physics of Solids. 2016;86:237 – 258.

[20] Nemat-Nasser S, Obata M. A Microcrack Model of Dilatancy in Brittle Materials. Journal of Applied Mechanics. 1988;55(1):24 – 35.

[21] Hogan JD, Farbaniec L, Mallick D, Domnich V, Kuwelkar K, Sano T, et al. Fragmentation of an advanced ceramic under ballistic impact: Mechanisms and microstructure. International Journal of Impact Engineering. 2016;102:47 – 54.

[22] Luo H, Chen W. Dynamic Compressive Response of Intact and Damaged AD995 Alumina. International Journal of Applied Ceramic Technology. 2004;1(3):254 – 260.

[23] Anderson Jr CE, Behner T, Orphal DL, Nicholls AE, Templeton DW. Time-resolved penetration into pre-damaged hot-pressed silicon carbide. International Journal of Impact Engineering. 2008;35(8):661 – 673.

[24] Shockey DA, Marchand AH, Skaggs SR, Cort GE, Burkett MW, Parker R. Failure phenomenology of confined ceramic targets and impacting rods. International Journal of Impact Engineering. 1990;9(3):263 – 275.

[25] Subhash G, Maiti S, Geubelle PH, Ghosh D. Recent Advances in Dynamic Indentation Fracture, Impact Damage and Fragmentation of Ceramics. Journal of the American Ceramic Society. 2008;91(9):2777 – 2791.

[26] Grady D. Impact failure and fragmentation properties of tungsten carbide. International Journal of Impact Engineering. 1999;23(1):307 – 317.

[27] Zinszner JL, Forquin P, Rossiquet G. Experimental and numerical analysis of the dynamic fragmentation in a SiC ceramic under impact. International Journal of Impact Engineering. 2015;76:9 – 19.

[28] Krell A, Strassburger E. Order of influences on the ballistic resistance of armor ceramics and single crystals. Materials Science & Engineering: A. 2014;597:422 – 430.

[29] Kimberley J, Hu G, Ramesh KT. A Scaled Model Describing the Rate-Dependent Compressive Failure of Brittle Materials. Dynamic Behavior of Materials. 2011;1:419 – 421.

[30] Hollenberg GW, Basmajian JA. Crack Propagation in Irradiated B4C Induced by Swelling and Thermal Gradients. J Am Ceram Soc. 1982;65(4):179 – 181.

[31] Migliori A, Sarrao J. Resonant ultrasound spectroscopy: application to physics, material measurement, and nondestructive evaluation. New York: Wiley; 1997.

[32] Migliori A, Darling T. Resonant ultrasound spectroscopy for materials studies and non-destructive testing. Ultrasonics. 1996;34(2-5):473 – 476.

[33] Autodesk Maya 2016 Documentation, Two-manifold and non-manifold polygonal geometry; 2016.

[34] Lorensen WE, Cline HE. Marching Cubes: A High Resolution 3D Surface Reconstruction Algorithm. Computer Graphics. 1987;21:163 –169.

[35] Chen WW, Song B. Split Hopkinson (Kolsky) Bar Design, Testing and Applications; 2011.

[36] Paliwal B, Ramesh KT. Effect of crack growth dynamics on the rate-sensitive behavior of hot-pressed boron carbide. Scripta Materiala. 2007;57:481 – 484.

[37] Brennan IV RE. (Dissertation), Ultrasonic Nondestructive Evaluation of Armor Ceramics; 2007.

[38] Damhof F, Brekelmans WAM, Geers MGD. Experimental analysis of the evolution of thermal shock damage using transit time measurement of ultrasonic waves. Journal of the European Ceramic Society. 2009;29(8):1309 – 1322.

[39] Shea VR, Hanson DR. Elastic Wave Velocity and Attenuation as Used to Define Phases of Loading and Failure in Coal. International Journal of Rock Mechanics and Mining Sciences & Geomechanics Abstracts. 1988;25(6):431 – 437.

[40] Phani KK. Correlation between ultrasonic shear wave velocity and Poisson's ratio for isotropic porous materials. Journal of Materials Science. 2007;43(1):316 – 323.

[41] Yu C, Ji S, Li Q. Effects of porosity on seismic velocities, elastic moduli and Poisson's ratios of solid materials and rocks. Journal of Rock Mechanics and Geotechnical Engineering. 2016;8(1):35 – 49.

[42] Asmani M, Kermel C, Leriche A, Ourak M. Influence of porosity on Young's modulus and Poisson's ratio in alumina ceramics. Journal of the European Ceramic Society. 2001;21(8):1081 – 1086.